THESIS FOR THE DEGREE OF DOCTOR OF PHILOSOPHY

Microwave Imaging for Muscle Rupture Detection

Laura Guerrero Orozco

Department of Electrical Engineering
Chalmers University of Technology
Gothenburg, Sweden, 2024

Microwave Imaging for Muscle Rupture Detection

Laura Guerrero Orozco
ISBN 978-91-8103-152-2

Acknowledgements, dedications, and similar personal statements in this thesis, reflect the author's own views.

Doktorsavhandlingar vid Chalmers tekniska högskola,
Ny serie nr 5610
ISSN 0346-718X
Department of Electrical Engineering

Chalmers University of Technology
SE-412 96 Gothenburg, Sweden
Phone: +46 (0)31 772 1000
www.chalmers.se

Cover:
Antenna array with muscle phantom laying on top, overlayed reconstructed image of the blood phantom inside.

Printed by Chalmers Reproservice
Gothenburg, Sweden, December 2024

To my father, whose guidance and lessons made this possible.

Abstract

Muscle injuries are common in sports like football, sprinting, and running, particularly affecting the hamstring muscles in the back of the thigh. Magnetic resonance imaging (MRI) is often used for diagnosis, but its high cost limits accessibility, leaving many patients without definitive diagnoses.

This work explores microwave imaging as an alternative for detecting muscle ruptures, offering a more affordable and accessible solution for earlier detection and better care. A microwave-based imaging system includes an antenna array, a measurement system, and an imaging algorithm. This research focuses on developing methods enabling design of a compact, low-cost system with repeatable and fast imaging capability.

In the first part of this study, measurement repeatability was investigated and improved using a monopole antenna with a lossy (conductive) gel to attenuate unwanted signals propagating outside the body. A software-defined radio (SDR) was also investigated as a low-cost, compact alternative to a Vector Network Analyzer (VNA). With a simple calibration strategy, the SDR achieved repeatability and accuracy down to more than -70 dB signal attenuation, proving it would be a viable option for muscle rupture detection.

The second part focused on reducing the measurement time while preserving imaging accuracy. The lossy gels in the antennas was found to improve the imaging accuracy, while a novel matched filter-based DMAS algorithm further improved the accuracy. This work also found that optimization of the number of measured transmission channels and measured frequency points enables faster measurements with minimal impact on image accuracy.

Finally, imaging experiments demonstrated that images could be successfully reconstructed with the SDR, combined with the DMAS algorithm.

In conclusion, this study provides the first proof of principle for a feasible, cost-effective microwave imaging system, offering a potential to further develop a portable alternative for muscle injury diagnostics.

Keywords: Microwave imaging, medical diagnosis, antenna system, muscle rupture, SDR, matched filter.

List of Publications

This thesis is based on the following publications:

[A] **Laura Guerrero Orozco**, Lars Peterson, Andreas Fhager, "Microwave Antenna System for Muscle Rupture Imaging with a Lossy Gel to Reduce Multipath Interference". Published in Sensors 2022, 22, 4121.

[B] **Laura Guerrero Orozco**, Lars Peterson, Andreas Fhager, "Muscle Rupture Microwave Imaging with a Lossy Gel to Reduce Multipath Interference". Published in 2023 17th European Conference on Antenna and Propagation (EuCAP), pp.1-5.

[C] Xuezhi Zeng, **Laura Guerrero Orozco**, "Measurement quality of a software defined radio system for medical diagnostics". Published in the Journal of Engineering-JOE, Volume 2022, Issue 12 December 2022 pages 1162-1172.

[D] **Laura Guerrero Orozco**, Lars Peterson, Andreas Fhager, "Microwave imaging with a reduced number of transmission channels in a semi-circular antenna array". Submitted to IEEE-JERM 2024.

[E] **Laura Guerrero Orozco**, Lars Peterson, Andreas Fhager, "Matched Filter Enhanced Delay Multiply and Sum for Muscle Rupture Microwave Imaging". Manuscript in preparation for submission.

[F] **Laura Guerrero Orozco**, Xuezhi Zeng, Andreas Fhager, "Microwave Imaging of Muscle Ruptures with Software Defined Radio". Manuscript in preparation for submission.

[G] Andreas Fhager, **Laura Guerrero Orozco**, Lars Peterson, "A Study on the Reduction of Frequency Points in Muscle Rupture Microwave Imaging in a semi-circular antenna array". Accepted for publication at the 19th European Conference on Antenna and Propagation, 2025.

Other publications by the author, not included in this thesis, are:

[H] **Laura Guerrero Orozco**, Andreas Fhager, "Microwave detection of muscle ruptures". *Medicinteknikdagarna*, 8-10 October 2024, Gothenburg.

[I] **Laura Guerrero Orozco**, Andreas Fhager, "Microwave Imaging System for Muscle Rupture Detection". *Medicinteknikdagarna*, 9-11 October 2023, Stockholm.

[J] **Laura Guerrero Orozco**, Andreas Fhager, "Study of a system for stable microwave image reconstruction applied to muscle rupture detection". *ESHO2022*, 34th Annual Meeting European Society for Hyperthermic Oncology, 14–17 September 2022, Gothenburg.

[K] Phase calibration of a software defined radio system for medical applications, "Xuezhi Zeng, and **Laura Guerrero Orozco**, Andreas Fhager". *2019 IEEE Asia-Pacific Microwave Conference, APMC 2019* Singapore, Singapore, 2019-12-10 - 2019-12-13.

Acknowledgments

I am deeply grateful to my supervisor Andreas Fhager. There are no words that can express how grateful I am to have been able to go on this journey with your guidance. You have been solid as a rock and it would have been impossible to accomplish this work without your expertise, insights, and constructive feedback. You have offered me not just academic guidance but also genuine encouragement during moments of uncertainty. Your mentorship has played a crucial role in shaping both my academic and professional growth.

I would like to express my sincere gratitude to my co-supervisor, Xuezhi Zeng, our journey started when I was just a master student doing my thesis with you. Thank you for believing in my potential. Without your support I would not be where I am now.

I am incredibly thankful to Lars Peterson for his essential contributions to this project. Without your medical knowledge and practical insights, this work would not have been possible.

I would like to extend my sincere thanks to my colleagues in the Biomedical Electromagnetics group: Hana Dobsicek Trefna, Mikael Persson, August Ekman and Alejandra, and former colleagues Samar, Morteza, Jan and Karan. A special thanks to my colleagues turned friends Moein, Mattia, Gabriel, Yara, Alvin, Ying, Ben and Rita. Thank you for your support and for all the times we have laughed together in the kitchen.

I would like to thank my friends Dmitrii (aka Dyma), Chouaib, Sara, Asta & Mauricio (Masta), Lewis, Roman, Guzal, Andre, and Boss for their unwavering friendship and support throughout this journey. I would also like to specially thank Fredric for his unwavering support, patience, and encouragement, which have been a constant source of strength for me. Another person I would like to mention is Naty, for guiding me through the tough times and helping me see things in a different light. I am deeply grateful to all of you for your belief in me and the positive impact you've had on my life.

Last but not least, I would like to thank my mom and brother back home for always supporting me. Your unwavering encouragement and belief in me have been my greatest strength.

I would like to dedicate this work to my father whose love, wisdom, and support shaped the person I am today. Though he is no longer with us, his influence remains a constant source of inspiration and strength. His unwavering faith in me, even in the toughest of times, gave me the courage to pursue

my dreams and never give up. I carry his memory with me every day, and this work is as much a reflection of his legacy as it is of my own. I miss him deeply, but I am forever grateful for the profound impact he had on my life.

Acronyms

OUT:	Object Under Test
SDR:	Software Defined Radio
VNA:	Vector Network Analyzer
DMAS:	Delay Multiply and Sum
UWB:	Ultra Wide Band
PLL:	Phase Locked Loop
SNR:	Signal to Noise Ratio
SCR:	Signal to Clutter Ratio

Contents

Part I

Overview

CHAPTER 1

Background

Imagine a world where every athlete, from recreational practitioners to Olympic champions, is provided with immediate, accurate injury diagnosis directly at the scene of an accident. In this work, the achievement of this potential reality is pursued through the application of microwave imaging technology for diagnosing muscle strains and ruptures.

Muscle injuries represent a significant challenge in sports medicine, constituting over 30% of cases encountered by clinicians [1]. They are among the most common injuries in sports medicine, yet they are frequently misdiagnosed and often receive insufficient treatment [2]. These injuries are particularly prevalent in high-intensity activities such as sprinting, running, soccer, and gymnastics [3], [4], with hamstring muscles being especially vulnerable [5].

Along with a physical examination, imaging plays a key role in diagnosing and managing athletes with muscle injuries [6]. The gold standard is magnetic resonance imaging (MRI) [7], [8]. However, the high cost and limited availability of MRI make it inaccessible to many, particularly for non-elite teams and recreational athletes. Therefore, in team sports, where multiple athletes may require assessment after each training sessions, MRI becomes an

unattainable luxury.

As an alternative, sonography is gaining popularity due to its lower cost and that it is portable [9]. Unfortunately, sonography needs a specialized operator and the result of the examination is highly operator dependent [8]. The operator needs specific knowledge of compartmental muscle anatomy as well as experience in assessing normal and abnormal muscle tissue during different healing phases [10], which is rare in many sports settings. Unfortunately this has limited the deployment of sonography outside centers specializing in sports medicine [11].

This leaves us with a diagnostic dilemma. While imaging is sometimes essential for correct diagnosis, it is often avoided due to its cost and limited availability, leaving countless athletes waiting in uncertainty. The issue is further compounded by the increasing number of individuals participating in recreational sports [12]. To add insult to injury, the prevalence of hamstring tears outside professional sports is not well documented [13]. As a result, these injuries, despite being equally painful and potentially debilitating, often go undiagnosed and untreated due to the associated costs and logistical challenges of current imaging methods.

However, the emergence of microwave imaging technology offers a promising solution to these challenges. In this work, a cost-effective and portable technology is being developed, addressing these challenges. It is envisioned that a device built with this technology could be widely accessible in sports clubs, training facilities, and competition venues, empowering coaches and medical staff to make quick, informed decisions, ultimately improving the quality of care for athletes at all levels.

1.1 Hamstring Anatomy and Injuries

Hamstring injuries are the most common type of injury in sports such as football, running, and activities involving jumping [2], [5], [14]. Due to the prevalence of hamstring injuries, the hamstring muscles are an ideal starting point when developing a diagnostic system. Therefore, the anatomy of hamstring muscles and the incidence of hamstring injuries will be discussed in this section.

The hamstring muscles play a crucial role in flexing the leg at the knee joint, extending the thigh at the hip joint, and contributing to leg rotation. These

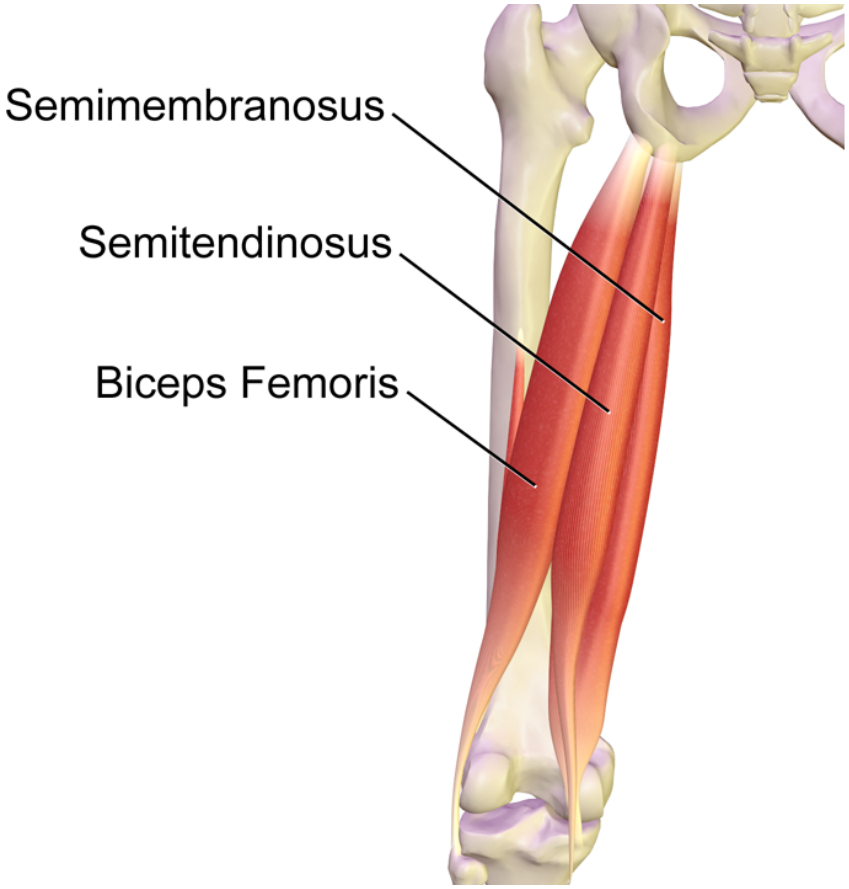

Figure 1.1: Illustration of the three muscles composing the hamstring:biceps femoris, semimembranosus and semitendinosus. Adapted from [17]

muscles are located in the posterior compartment of the thigh [15]. Figure 1.1 shows the three long muscles in the posterior compartment of the thigh that compose what is known as the hamstring: the biceps femoris caput longum, biceps femoris caput breve, semimembranosus and semitendinosus muscles.

One explanation for the high incidence of injuries in the area is that this muscle group functions between two joints, therefore it needs to stretch at more than one point [16]. Additionally, the hamstring muscles have a muscle-tendon junction for almost the entire length of the muscles creating weak spots in the muscle and making it possible to have a muscle strain at any point in the muscle [15].

Epidemiology of Hamstring Injuries in Athletic Populations

Hamstring injuries present a significant and persistent challenge across various athletic disciplines. A study examining injury trends in English professional football over 11 seasons revealed that muscle strains constituted 49% of all injuries. Among these, hamstring injuries were the most common, representing 17% of all injuries and 34% of muscle injuries [18]. Similarly, Ekstrand et al. found comparable results in their study of 23 teams selected by the Union of European Football Associations (UEFA), identifying thigh strains as the most prevalent injury subtype, accounting for 17% of all injuries [19].

An analysis of injury patterns in English professional football, covering both Premier League and Football League competitions, revealed that hamstring strains constituted 12% of all reported injuries over two consecutive seasons [20], making them the most frequent injury type. English football clubs experience an average of five hamstring injuries per season, a figure closely aligning with data from Australian football, where clubs report a mean of six hamstring strains per season [21].

In elite track and field, lower limb injuries dominate, accounting for 92.7% of all injuries, with hamstring injuries being the most common (33.4%) [22]. This trend is further supported by data from the International Association of Athletics Federations (IAAF) World Championships, which shows that thigh injuries are the most common injury (Figure 1.2) [23].

Hamstring injuries predominantly affect the biceps femoris and semimembranosus muscles, with the biceps femoris being involved in approximately 66% of cases [2]. A significant portion, around 33%, also involves concurrent trauma to both the biceps femoris and the semitendinosus muscles. In elite track and field, 75% of all hamstring injuries occur in the biceps femoris , with the musculotendinous junction affected in 93% of these cases [24].

One of the most concerning aspects of hamstring injuries is their high recurrence rate, ranging from 12% to 43% [2], [20]. This propensity for relapse poses a significant challenge for injury management and rehabilitation [20], [25]. Additionally, these injuries contribute to prolonged athlete downtime, affecting individual performance and team dynamics [20], [21]. These injuries also impact athletes on multiple levels, physically, psychologically, and socially, leading to both short and long term consequences for musculoskeletal function, athletic performance, and career progression [26].

Severe cases of hamstring injury may require up to 12 months for complete

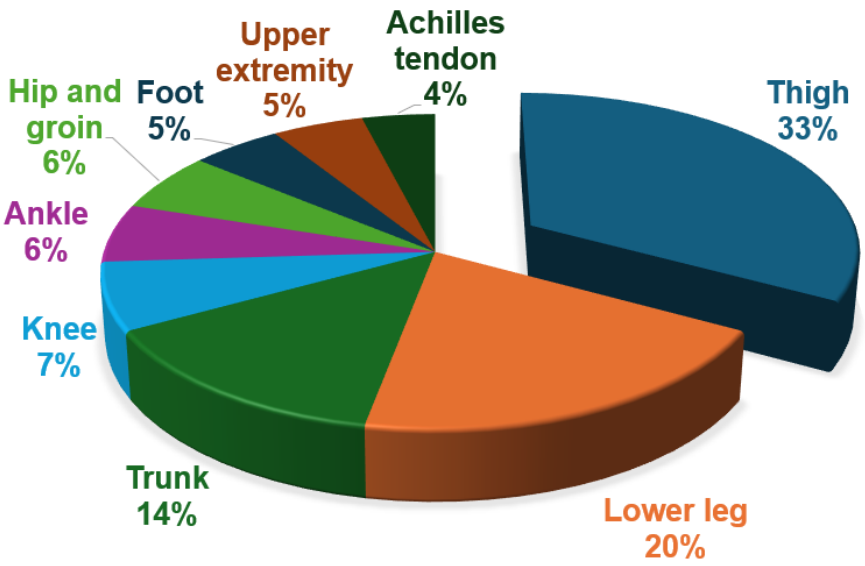

Figure 1.2: Injury location in male athletes during IAAF World Championships in Athletics. Figure created using data from [23].

recovery and rehabilitation [25]. In rugby union, hamstring injuries result in a mean of 17 days of lost playing time, with recurrent injuries often necessitating longer recovery periods compared to initial injuries [27]. Similarly, track and field athletes experience recovery times ranging from 2 to 6 weeks [24], underscoring the variability in recovery across different sports.

1.2 Understanding Muscle Injuries

In this section, the structure and composition of muscle tissue will first be explored, followed by a discussion of common types of muscle injuries frequently encountered in sports and physical activities, and then current diagnosing methods will be discussed.

Muscle tissue is composed of bundles of elongated cells known as muscle fibers [28]. Each muscle fiber contains myofibrils, which are the structures responsible for contraction. These fibers are organized into larger bundles, fascicles. Multiple fascicles come together to form the muscle tissue as we recognize it (Figure 1.3).

Muscle injuries can be broadly categorized into strains (ruptures) and hematomas

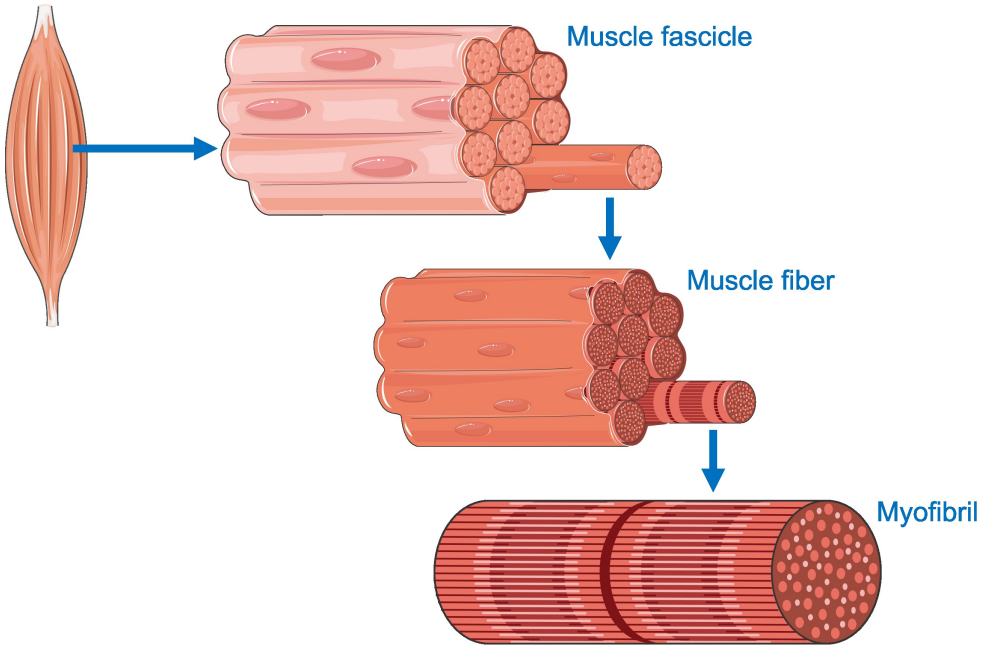

Figure 1.3: Illustration of muscle belly composition: bundles of muscle fiber form fascicles and bundles of fascicles from the muscle tissue. Source [29]

(bleeding) [2].

Muscle Strains: Grading and Biomechanical Aspects

Muscle strains or ruptures refer to the partial or complete rupture of the muscle fibers. Healthy muscle fibers function like elastic bands, stretching and contracting during movement. However, repetitive overuse or sudden forceful actions can cause these fibers to stretch beyond their limits, leading to injury. Muscle strains are classified into three grades depending on the severity of the injury [7](Figure 1.4). Grade I represents a minimal injury, with less than 5% of the muscle fibers torn. Grade II is a partial tear, involving between 5-50% of the muscle, which can often be treated with physiotherapy starting a couple of days after the injury. Grade III is a complete rupture, which typically requires surgical treatment [30].

There are two main reasons for muscle ruptures [2]:

- **Distension ruptures**: These occur due to overstretching of the muscle, typically from sudden, unexpected movements such as slipping or

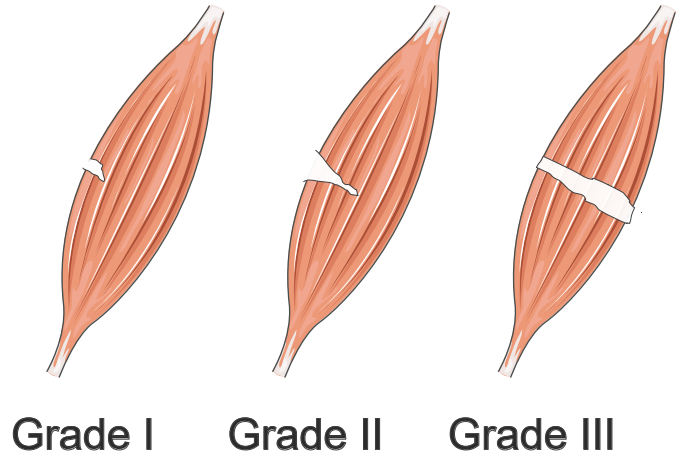

Figure 1.4: Illustration of muscle belly with different grades of injury. Adapted from [29].

lifting a heavy object, in sports this can happen for example when a football player suddenly starts running to catch the ball. Distension ruptures tend to occur at the muscle-tendon junction or in superficial muscle layers, often affecting muscles that span two joints, such as the hamstrings.

- **Compression ruptures**: These are caused by direct trauma, where the muscle is forcefully compressed against a bone. For instance, a knee-to-thigh impact during a football game can lead to this type of rupture. Compression injuries are often deep and can cause significant bleeding within the muscle.

Intramuscular and Intermuscular Hematomas

When a muscle fiber ruptures, the capillaries within it also break, leading to a bleeding and the formation of a hematoma [31]. The severity of this bleeding can vary significantly, and this variation is closely tied to two key factors [2], [32]: the blood flow to the muscle and the activation status of the muscles involved.

Muscle bleedings come in two main types: intramuscular and intermuscular [33]. Sometimes, a combination of both can occur.

- **Intramuscular bleeding**: occurs when blood is confined within the

muscle fascia, the tough outer layer that encases the muscle [2]. This type of bleeding is typically caused by overstretching or direct impact. As blood accumulates, it increases pressure inside the muscle.

- **Intermuscular bleeding**: occurs when the fascia is ruptured, allowing blood to escape between muscles and their surrounding fascia [33]. This usually results in visible swelling and bruising. In some cases, an intramuscular bleed can progress into intermuscular bleeding if the pressure causes the fascia to tear.

Intramuscular hematomas are often considered more problematic than intermuscular ones. It is frequently recommended to drain these internal bleeds to prevent complications such as abnormal bone formation or excessive scarring [32]. Although less common, intramuscular hematomas can also lead to compartment syndrome, a serious condition caused by increased pressure within the muscle compartment.

Diagnosis and Imaging of Muscle Injuries: Current Approaches and Challenges

Diagnosing and assessing muscle injuries is a complex challenge, as these injuries can differ significantly in severity, location, and recovery time. While most injuries are managed conservatively without imaging [16], the necessity of imaging remains a topic of debate among clinicians [24].

Initial diagnosis typically begins with a clinical evaluation, ideally conducted within 1-2 days of symptom onset [2]. This evaluation encompasses a range of assessments, including inspection for bruising, gait analysis, palpation for tenderness, pain during hip flexion, and comparison of active range of motion between the injured and uninjured limbs [24]. The hallmark symptom is intense, knife-like pain following sudden movement, often accompanied by inflammation and edema [34].

However, the limitations of clinical evaluation alone are evident. The potential for misdiagnosis exists due to the overlap of symptoms with other conditions. For example, minor-grade hamstring injuries have considerable overlap in clinical symptoms with injuries involving referred pain (when the pain felt in one part of the body is actually caused by pain or injury in another part of the body) [35]. This underscores the value of imaging techniques in achieving accurate diagnoses.

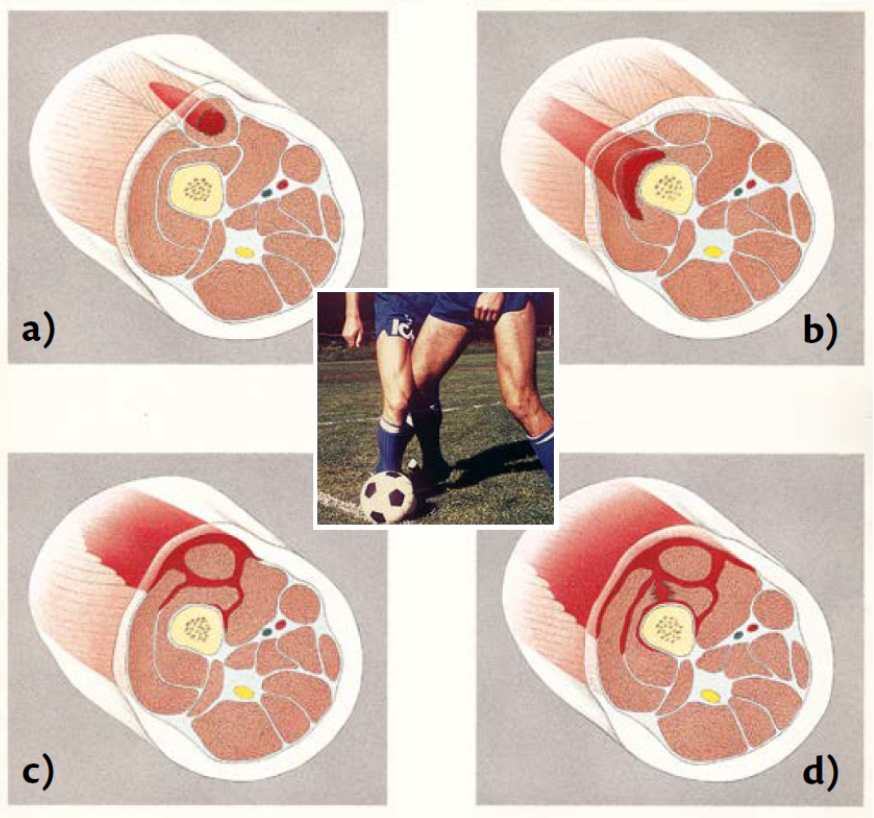

Figure 1.5: Muscle trauma caused by external impact, such as a knee to the thigh during football, can lead to various bleeding patterns: **(a)** superficial intramuscular bleeding,**(b)** deep intramuscular bleeding,**(c)** Intermuscular bleeding, and **(d)** deep intramuscular bleeding transitioning to intermuscular bleeding after fascia rupture. Used with permission from the author [2].

Magnetic Resonance Imaging (MRI) offers detailed visualization, capable of identifying injuries affecting as little as 5% of the muscle [2]. However, simpler clinical techniques would be preferred from a cost and availability point of view [36]. Ultrasound, while more economical and accessible, is sometimes omitted for grade I and II injuries to minimize costs [24]. In such cases, the diagnosis relies solely on a physical examination. Additionally, there is a time constraint when imaging, ideally coinciding with the clinical evaluation window of 1-2 days post-injury.

Imaging is more likely to be performed early in elite athletes, in cases where there is severe pain [16]. Conversely, minor injuries are usually not deemed

important enough to afford the cost of imaging and thus are also less likely to be recorded in literature [37]. This approach, however, may overlook the significance of minor injuries (grade I and II) in predisposing athletes to more serious re-injuries.

The prevailing diagnostic approach reveals a significant deficiency in muscle injury management, especially concerning minor strains that subtly compromise athletic performance without causing overt functional limitations. This gap presents an opportunity for emerging technologies, such as microwave imaging, which could offer a cost-effective solution for comprehensive assessment of all injury grades, potentially improving long-term outcomes and reducing re-injury rates.

1.3 Microwave Imaging: Emerging Technology in Muscle Rupture Detection

Microwave-based imaging and diagnostics have gained increasing prominence in recent years, emerging as a potential competitor or complementary technique to current imaging modalities used for muscle rupture detection. Historically, microwave imaging has been used in long-range applications like marine radars and weather radars but in recent years short-range applications have gained attraction, an example of this is surveillance for concealed weapons in airports [38]–[40]. This shift has opened avenues for exploring microwave imaging in biomedical contexts.

There are two reasons why this technology is interesting for biomedical applications. The first is the operating frequency range. The technology exploits electromagnetic radiation that goes from several hundred MHz to several hundred GHz with wavelengths (λ) ranging from 1 m to 1 mm. These wavelengths are similar to dimensions inside the body [41], [42]. This allows for enough resolution to create an image presenting a map related to the dielectric properties in a region of the body. The choice of an appropriate frequency range to use in this application is vital, a higher frequency gives better imaging resolution, but it will at the same time result in a more shallow signal penetration depth into the body. Therefore, frequencies above 10 GHz might not give much information about the deeper part of the body making them more appropriate for surface applications instead.

The second is that there is a contrast in the dielectric properties, permit-

tivity (ϵ_r) and conductivity (σ), that is naturally found in different tissues in the body [43], [44]. This inherent contrast facilitates the differentiation of various tissue types and the detection of abnormalities.

The potential of microwave imaging extends beyond muscle rupture detection. Over the years, it has been explored in various medical diagnostic applications, including breast imaging [45]–[47], brain imaging [48], [49], kidney imaging [50], cardiac imaging [51], bone disease measurements [52], [53], compartment syndrome detection [54], and recently in applications involving ligament tears like knee imaging [55] and rotator cuff tears [56].

Properties of Leg Tissue in the Microwave Region

The permittivity in the MHz to GHz range is mostly dependent on the water content in the tissue, for example, the permittivity of low water content tissues like fat and tumors is lower than high water content tissues like muscle and skin [43], [44], as shown in Figure 1.6a. On the other hand, conductivity depends mainly on the presence of ionized atoms due to different dissolved substances, like salts or sugars in the tissue (Figure 1.6b). Additionally, the dielectric properties of tissues exhibit strong dependence on frequency (frequency dispersion) in the RF and microwave bands.

Figure 1.6 reveals a dielectric contrast between muscle and blood, which will be exploited in our diagnostic system. By leveraging the presence of blood associated with muscle injuries, the goal is to design a prototype capable of detecting bleeding within muscle tissue.

1.4 Aim and Thesis Outline

The aim of this project is to explore the use of microwave imaging for diagnosing muscle ruptures by developing a radar-based imaging system. In Papers A and B, the use of lossy gels is investigated to attenuate multipath signals and improve image quality, while employing low-profile antennas. Paper D will focus on evaluating the effectiveness of circular versus semi-circular antenna arrays, as well as determining the optimal number of transmission channels required for adequate image reconstruction. Additionally, Paper E will explore a method inspired by matched filters to enhance image quality. The applicability of Software Defined Radio (SDR), commonly used in wireless

communications, in medical imaging will be examined in Paper C. Paper F will show image reconstructions obtained using our calibration strategy for the SDR. Finally, Paper G will evaluate the number of frequency points needed for reconstructions.

The thesis contains two parts. Part I has 5 chapters. Chapter 1 provides a background for a better understanding of muscle ruptures and current diagnosing methods and states the aim of the thesis. Chapter 2 gives a brief overview of measurement systems as well as antenna arrays, the antenna used in this project is introduced as well as some results obtained using the lossy gel. Chapter 3 the different approaches to microwave imaging are explained with some experimental image reconstructions shown. Chapter 4 presents a summary of the appended papers. Finally, chapter 5 concludes the thesis and discusses possible directions for future work. Part II contains the main contributions of the author in the form of appended papers.

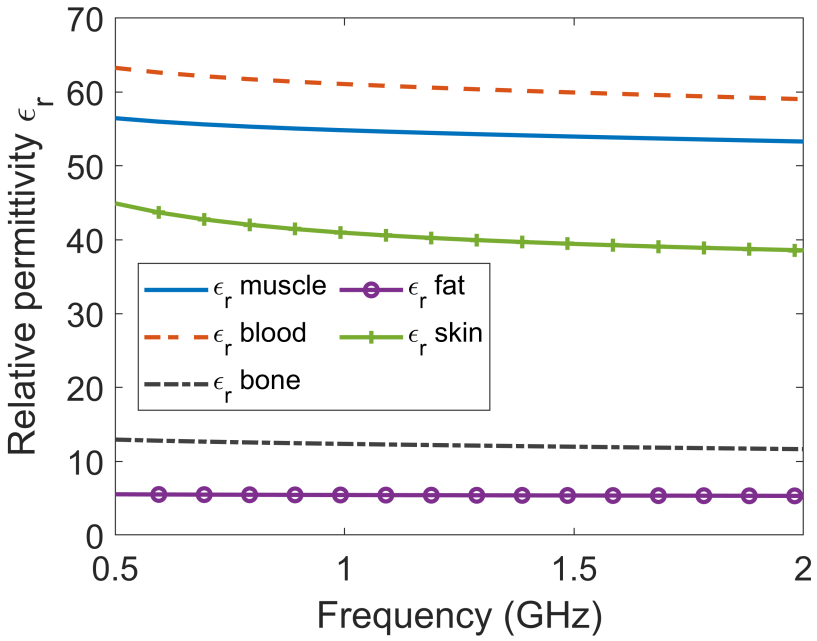

(**a**) Relative permittivity ϵ_r

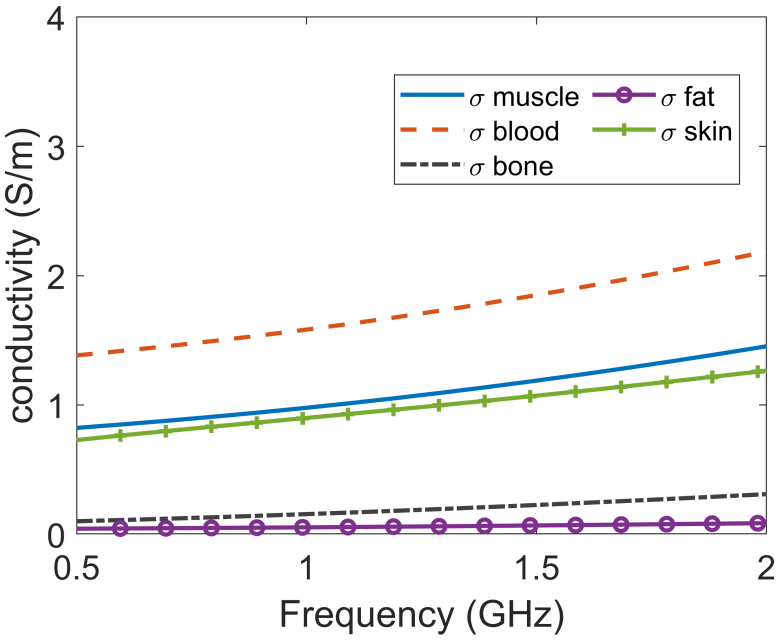

(**b**) Conductivity σ(S/m)

Figure 1.6: Permittivity and conductivity of different tissues in the leg. This image was created using data from [44].

CHAPTER 2

Experimental Systems

There are three components in a microwave imaging system: a measurement system, an antenna array and an imaging algorithm. The measurement system handles signal transmission and reception to and from the antennas, while the antenna array enables the signals to couple into the object under test (OUT) and captures the scattered signals. A computer executes the imaging algorithm and processes the raw data to reconstruct the image.

This chapter is divided into two parts. The first part provides a brief introduction and discussion of state-of-the-art measurement systems and antenna arrays. The second part, presents the main contributions and experimental results of this thesis, focusing on the practical implementation and evaluation of the proposed microwave imaging system and antennas.

Part I: Overview of Measurement Systems and Antennas

In microwave imaging, a measurement system refers to the setup used to generate, modulate, and detect microwave signals. It typically consists of several components working together to send and receive electromagnetic waves. These systems can be based on single frequency, multiple frequency, or ultra-wide band (UWB) data, Where UWB refers to a bandwidth greater than 20% of the center frequency or 500 MHz. The measurements can be carried out using frequency domain systems or time domain systems. There are many examples of each type of system used in previous research studies, and some examples are [57]–[61].

Most of the research studies published so far aim at proof-of-principle of a particular diagnostic application. A majority of them have been conducted with costly and bulky lab equipment like VNAs or oscilloscopes. However, more compact and low-cost measurement systems are desired to facilitate clinical adaptation. This is why many research groups have started working on minimizing systems using either compact commercial instruments or custom-built systems [49], [62]–[65].

For example, a 16-port VNA like the Rohde & Schwarz ZNBT8, which has been used in the studies in this thesis, can cost over 1 million SEK, depending on the configuration. It's a powerful tool in the lab, but with a weight approaching 40 kg, it is not an easily portable device. A two-port VNA is more portable with a typical price range at around 100,000 SEK. For many applications this is still too high to enable a widespread clinical use, especially for pre-hospital applications.

To make our microwave imaging systems both affordable and portable, alternative measurement options must be explored. One promising solution is the Software Defined Radio (SDR), which could significantly reduce both the cost and size of the measurement system. Priced at about 30,000 SEK (for the NI 2901 system used in the studies in this thesis), an SDR system is seen as a much more cost-effective alternative. As a result, efforts have been made to adapt and integrate SDR technology into the microwave imaging application.

In the following subsections the various measurement technologies and systems are introduced and discussed.

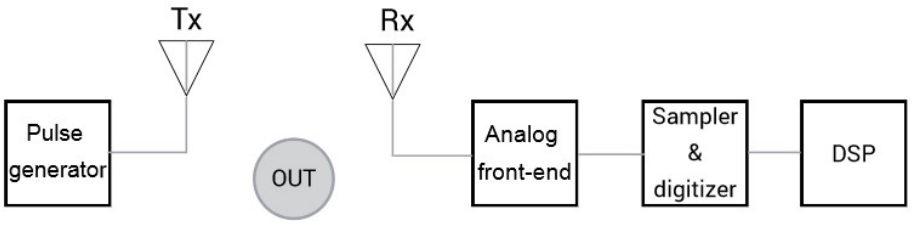

Figure 2.1: System block diagram of a time domain measurement system for microwave imaging.

2.1 Time Domain Systems

In time-domain systems, the object's response is measured as a function of time. A pulse generator creates the transmitted signal, which interacts with the object. The receiving antenna then captures the resulting time-domain response, which is subsequently sampled and digitized for image reconstruction, as illustrated in Figure 2.1. In such systems, high-speed real-time oscilloscopes or sampling oscilloscopes are often used as receivers.

Time-domain systems, which are often custom-built rather than readily available like VNAs, are used in applications where fast acquisition is needed, such as medical imaging. Real-time oscilloscopes, for example, can capture UWB data in a single measurement, significantly reducing the acquisition time. Numerous experimental systems utilizing time-domain measurements have been proposed for various imaging applications [57], [58], [66].

One notable application of UWB data is in breast cancer imaging, where efforts have been made to miniaturize the measurement systems. For example, an integrated stepped-frequency continuous-wave (SFCW) UWB radar transceiver was developed for a breast imaging system [62]. Another approach involved replacing bulky pulse generators with integrated circuit pulse radios, significantly reducing the size and cost of the system [64]. Additionally, advancements in microwave tomography have focused on miniaturization, with long-term goals of developing system-on-chip solutions [63], [67].

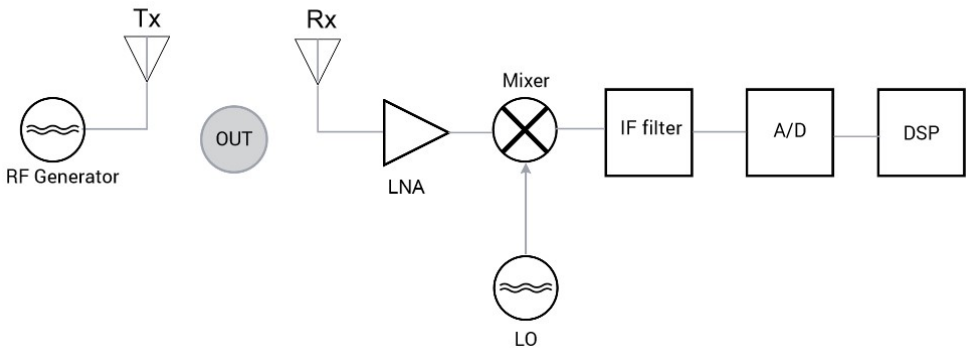

Figure 2.2: System architecture of VNA for microwave imaging.

2.2 Frequency Domain Systems

Another approach to microwave imaging is through frequency domain measurements. In here the object's response is measured as a function of frequency. This is done by sending single frequency test signals in stepped manner sequentially until covering the desired bandwidth. If needed, a time domain pulse can be synthesized with a Fourier transform from the frequency domain scattering data obtained [68], [69].

A commonly used frequency domain measurement system is the vector network analyzer (VNA). The architecture of a VNA-based system is shown in Figure 2.2. In this method, an RF generator illuminates the OUT, and the response is captured, amplified, down-converted to an intermediate frequency (IF), filtered, digitized, and processed to extract amplitude and phase.

VNAs are supported with powerful measurement platforms as well as calibration functions that can provide ready-to-use, high-accuracy solutions for experimental use, making them highly relevant in research [59]–[61], [70], [71]. One disadvantage is that VNAs suffer from long settling times due to the need for narrowband IF filters or slow synthesizers. Therefore, the measurement speed can be quite limited, especially when performing UWB measurements at a large number of frequencies.

Recent developments in compact VNAs have addressed some of these limitations, offering more portable solutions for clinical and experimental use. For instance, portable VNA systems have been successfully employed in clinical trials for stroke detection [49], [72] and phantom experiments targeting head

injury detection [65].

2.3 Software defined radio

Software Defined Radio (SDR), refers to a wireless communication technology in which the transmitter modulation is generated or defined by a computer [73]. Large parts of the waveform are defined in software, giving the flexibility to change the waveform within certain bounds, also extend the flexibility to multi-band transmission. The demand for flexibility in communication applications has made the SDR a technology that is useful in many areas within wireless systems. It is very interesting in particular for the military sector, an area that has been the driving force in the development of this technology [74]. As mentioned before, for pre-hospital diagnostics systems to be viable, small, cheap, and accurate system are needed. SDRs are very compact in size and are significantly lower in cost compared to a VNA, therefore it is interesting to explore if such systems could replace VNAs in microwave diagnostic applications.

In [75], Marimuthu et al. proposed a monostatic SDR-based UWB head imaging system where they demonstrated image reconstructions of simple objects. In [76], they developed a multistatic imaging system composed of an SDR board and a switching matrix. Meaney et al. reported a sixteen-channel tomographic system made up of nine SDR boards [77].

As a device made for wireless communications the SDR cannot be completely classified as a frequency domain system or a time domain system since it presents qualities found in both types of systems, but due to its flexibility, it has the possibility of being operated in a way that resembles a frequency domain system.

Figure 2.3 shows a typical single-channel SDR system [78]. On the receiver side, it has many of the same components as the frequency-domain system (Figure 2.2). A main difference is that the A/D converter is placed after the amplifier (VGA), and the down-conversion is made digitally in the DDC, unlike the analog approach used in frequency-domain systems.

Also, with an SDR, wide-band measurements can be performed using a stepped frequency approach. Due to the variable gain in both transmitters and receivers, the system can potentially provide a high dynamic range. This makes the system appealing for medical applications where the signal strength

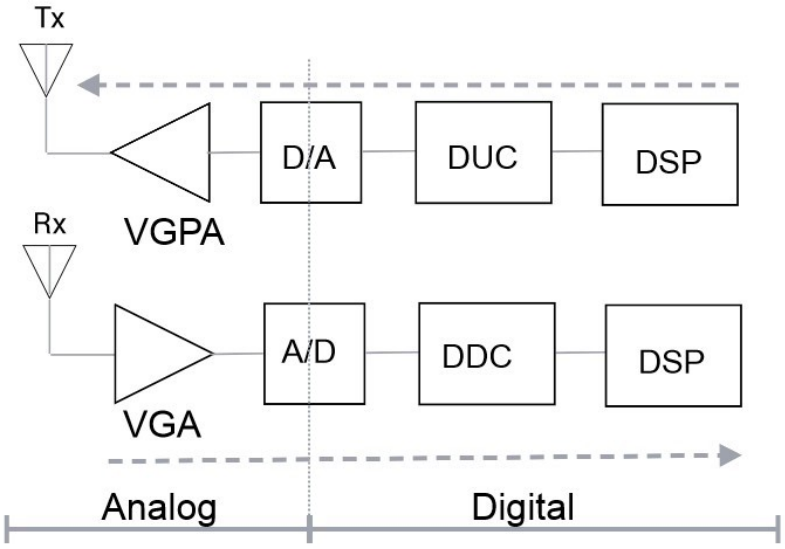

Figure 2.3: Simplified system architecture of SDR.

varies.

2.4 Antennas and Antenna Arrays

The bridge between the measurement system and the media where the signals will propagate, in our case the leg, is the antennas. They are used as both transmitting and receiving elements. Various types of antennas have been proposed for microwave imaging applications across different parts of the body [45], [79]–[84]. These antennas are typically grouped in different geometric patterns, this is called an antenna array, and a circular array is the most common configuration for biomedical applications. However, other configurations, such as half circles or half spheres, are also feasible depending on the specific imaging requirements [79], [85]–[88].

In a standard measurement system, an antenna array, as illustrated in Figure 2.4, surrounds the OUT, positioned at the center of the array. Each antenna can function as both a transmitter and a receiver. Typically, one antenna transmits while the others receive, and this process is repeated for each antenna, ensuring all possible combinations of transmitting and receiving antennas are used.

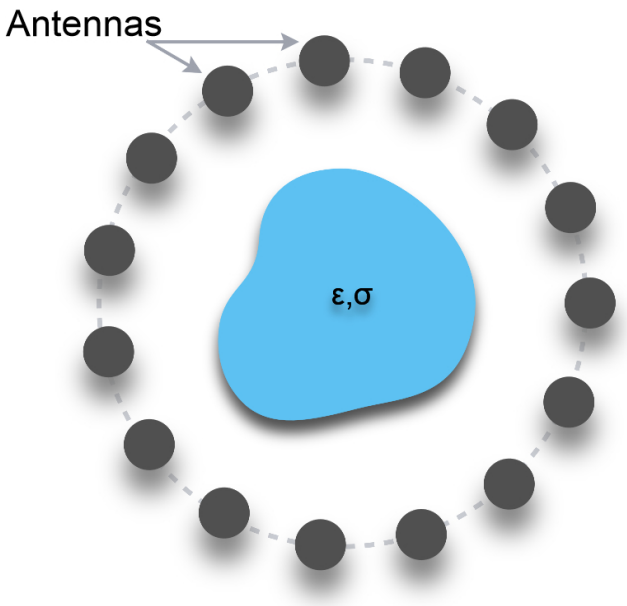

Figure 2.4: Schematic representation of an imaging system.

Multipath signals

The interesting parts of the signals are those that originate from the transmitter, enter into the OUT, scatter within the OUT to finally leave the OUT and get picked up by the receivers. However, as shown in Figure 2.4, the antennas are positioned close to one another, which leads to additional signal paths apart from those passing through the OUT. These include reflections from parts of the antenna system and surrounding environment, direct propagation between antennas or even cross-channel leakage within the electronic system. All these signals are referred to as multipath signals and are undesired as these signals tend to be strong and, even with small variations between measurements, can introduce unpredictable inconsistencies. As a result, image reconstruction becomes prone to artifacts, as discussed in Papers A and B.

The unwanted multipath signals carry no useful information from the OUT [89]. These signals are particularly problematic because they cannot be easily filtered out or calibrated out; they originate from the same source as the desired signals, share the same frequency, and appear as interference. This is especially challenging in near-field biomedical applications, where the useful signals are heavily attenuated by biological tissue. In such cases, multipath propagation can overwhelm the weaker, desired signals, causing them to be drowned out by the stronger, unwanted signal paths.

Additionally, the dielectric properties of biological tissue differ significantly from those of air, leading to substantial reflections at the interface between the air and the OUT. This results in a lower amount of signal power penetrating into the OUT.

To reduce the impact of unwanted signals and reflections from surrounding structures, it is important to maximize the power that penetrates the body while minimizing the energy that propagates outside the OUT. Two approaches have been proposed to enhance signal penetration [39]: designing antennas with precise impedance matching or using coupling liquids that improve impedance matching and attenuate energy outside the OUT, thus increasing the efficiency of energy transfer into the body.

Directive Antennas

In this approach, both off-body and on-body antennas are designed to maximize the energy coupled into the OUT while minimizing the power radiated in other directions. By using antennas with good impedance matching and directing the main radiation lobe towards the body, multipath effects caused by waves traveling outside and around the antennas are minimized. Several examples of such antenna designs exist in the literature [45], [79]–[84], [90], including applications like the evanescent field applicator for contactless microwave breast diagnostics in air [91].

These antennas typically offer advantages such as broader operating bandwidths, unidirectional radiation patterns with high gain, and compact sizes, making it possible to include a sufficient number of antennas in an imaging system.

Unfortunately, this increased performance comes at the cost of added complexity, which poses challenges for microwave tomographic algorithms. Larger, more geometrically complex antennas require more memory and therefore

longer simulation time. As a result, these antennas are less suitable for tomographic algorithms but are more appropriate for radar-based algorithms [59], [92].

Coupling Liquids

Another approach is to use coupling liquids to reduce the contrast between the surrounding medium and biological tissue. The first experiments using coupling media were conducted by Larsen and Jacobi, who used water as the coupling medium [93], [94]. Since then, a variety of liquids have been explored [95]–[98]. Some systems have used saline solutions or mixtures of glycerine and water to create a lossy coupling bath [59], [99]. By immersing both the antennas and the OUT in this lossy medium, unwanted multipath signals are effectively attenuated [97], [99], [100].

At the same time, coupling liquids help provide impedance matching between the antennas and the object, which maximizes the energy coupled into the OUT. Additionally, the use of lossy liquids broadens the operating bandwidth of the antennas due to resistive loading. This allows for the use of low-profile antennas, such as monopoles or dipoles, across a wide frequency band [101]. These types of antennas are less complex to model and are, therefore, more suitable for tomographic imaging.

Part II: Contributions and Measurement Results

This section summarises and discusses the contributions and experimental results of this thesis, starting with an in-depth examination of the measurement quality of the software-defined radio (SDR). Measurement challenges such as phase instability and limited channel isolation are addressed. The section further presents the antennas, with a focus on the strategy for minimizing multipath signals by using a high-loss gel.

2.5 Measurement Quality of SDR

The applicability of software-defined radios (SDRs) in microwave imaging systems is heavily influenced by their ability to consistently deliver precise amplitude and phase measurements. These quantities are critical for capturing accurate object responses and ensuring high-quality imaging results. However, SDR-based systems often encounter challenges such as phase instability, low channel isolation, and signal leakage, all of which can compromise the measurement fidelity. This section discuses the performance of the SDR, addressing these challenges through calibration techniques, enhanced setups, and experimental validation. The discussion is based on findings from Papers C and F, where the feasibility of SDRs in practical imaging scenarios was investigated.

In Paper C, the measurement quality of a SDR is explored. This system is a two-channel USRP 2901 from National Instruments [102], which is equivalent to the Ettus Research USRP B210 board. A common problem in software-defined radios (SDRs) when applying them to biomedical applications is the use of two different phase-locked loops (PLLs) that generate the carrier frequencies for the transmitter and receiver, respectively. Although both PLLs use the same reference input clock, their output clock signals are not synchronized. As a result, the phases of the generated clocks are random and may vary between measurements. Consequently, the measured phase will also be random and cannot be correlated with the object's response. A calibration strategy to stabilize these phase measurements is presented in Paper C, which creates a reference channel and an object channel using the two receivers, as they share the same PLL and, therefore, the generated clock phase is the same for both receivers.

Figure 2.5: The SDR connected to the ZTVX-16-18-S Blocking Switch Matrix. This is the measurement set up used in paper F.

One of the main challenges with SDR-based systems is also the limited isolation between transmission channels. The accuracy of our calibration strategy depends on the isolation between the reference and object channels. Additionally, the efficacy of this solution relies on the performance of both receivers and is largely impacted by significant signal leakage from the transmitter to the receivers.

In Paper F, imaging experiments were conducted using an SDR-based measurement system with a muscle phantom representing the leg and a blood phantom simulating blood from a rupture. The object channel was connected to the 8 antennas in the array using the ZTVX-16-18-S Blocking Switch Matrix from Mini-Circuits, which allowed switching between antennas during measurements. This setup is shown in Figure 2.5. (The antenna array will be further described in the next section.)

Figure 2.7a shows the measured power in the object channel before any calibration was applied. The measurements record the power levels in the different transmission channels, ranging from the closest antennas (R21) to the farthest (R81). Note that this is the received signal, not to be confused with the S-parameters.

Given the increasing distance between the antennas, it is expected to see a gradual drop in signal strength due to the longer transmission paths and corresponding attenuation. However, after the first channel (R21), the power levels

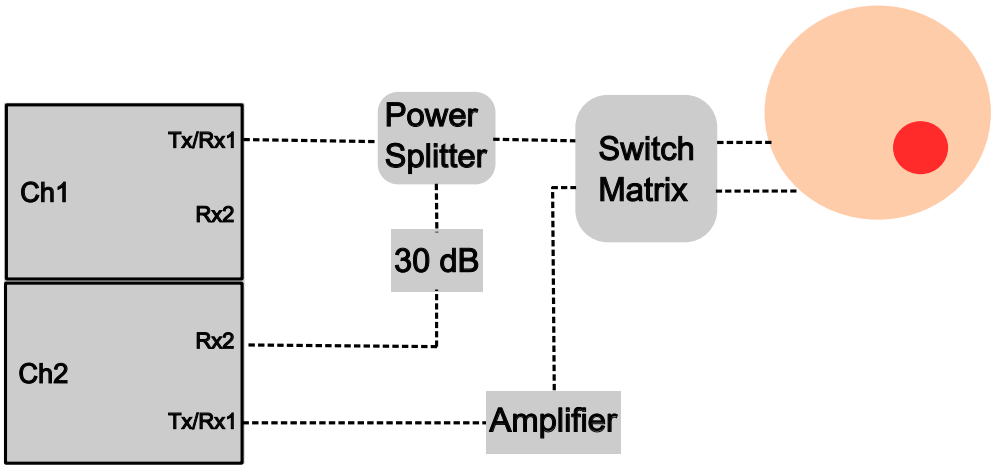

Figure 2.6: The measurement setup for a calibrated measurement showing the position of the amplifier stage between the antenna array and object receiver. In this illustration the object receiver is Rx1 and reference receiver is Rx2 in channel 2. This image is from Paper F.

for subsequent channels appear to overlap each other, which is unexpected.

The overlapping of power levels suggests an isolation issue, as described in Paper C. It was demonstrated that the noise floor was lower than the signal amplitudes observed in these measurements. The overlapping signals are likely a result of leakage from the transmitted power into the object channel, overpowering the signal received from the measured object.

To mitigate this problem, an amplifier was introduced between the antenna array and the object receiver, as shown in Figure 2.6. The purpose is to amplify the received signal level such above the internal isolation limit of the SDR. After amplification, the measured power in the object channel (shown in Figure 2.7b) presents a much clearer distinction between channels. The signals from channels R21 and R31 are now clearly separated, and small variations are visible across the channels until R61 is reached. However, channels R71 and R81 still overlap, indicating that at these points, the leakage from the transmitter remains stronger than the received signal from the object. Possibly this problem could be solved with even higher amplification levels in the receiver channel.

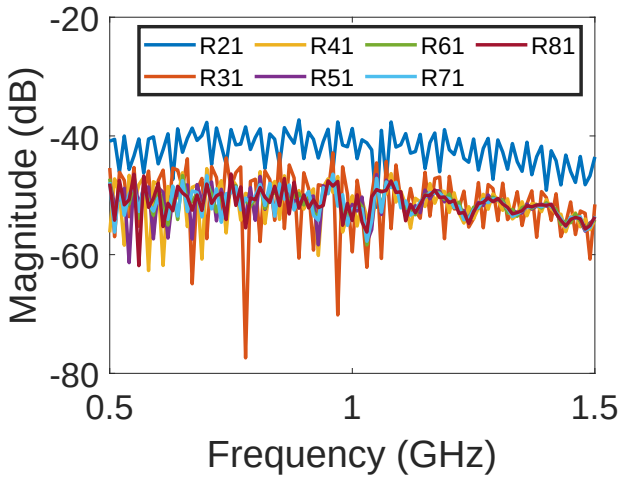

(**a**)

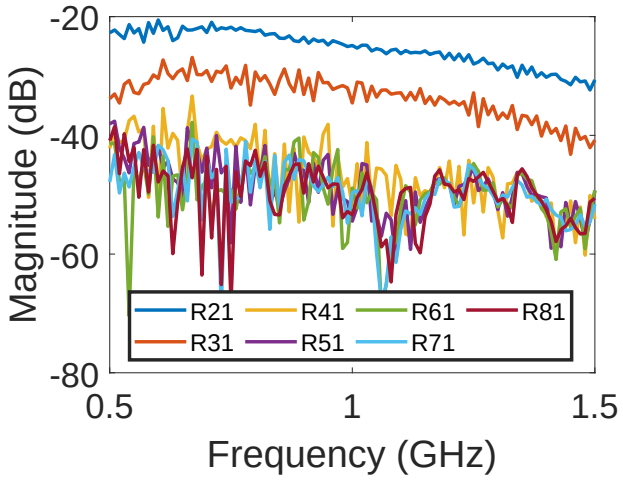

(**b**)

Figure 2.7: Measured power in object channel (SDR): (**a**) using no amplification; (**b**) adding an amplification stage. This image is from Paper F.

2.6 Antennas for muscle rupture detection

Although radar based imaging algorithms might provide effective diagnostics, our design choice has been to consider solutions that also enable tomographic imaging. Dielectric properties reconstructed with quantitative tomographic imaging, may offer valuable insights for diagnosing muscle ruptures. To streamline the processing time of tomographic algorithms, simple antennas like monopoles were opted for, as they reduce the complexity of numerical models and optimize the overall algorithm performance. This is the reason why a design using simple monopole antennas is suggested in this work.

Simple monopole antennas have shown to be effective in applications aimed at quantitative image reconstruction [59], [103], [104]. Hosseinzadegan et al. [59] developed a fast reconstruction algorithm based on the 2D discrete dipole approximation, which takes advantage of the simplicity of monopole antennas by efficiently modeling them as line sources. Additionally, a lossy coupling bath, made of water glycerin mixtures, ensures the reduction of unwanted multipath signals, for example, scattering from the wall of the imaging tank and the antenna elements themselves.

However, a liquid coupling bath is not practical for muscle rupture applications, as it would require the patient's leg to be fully immersed in the bath during measurements. Our aim was to explore antenna design principles tailored for muscle rupture imaging that would not require immersion of the entire leg in a liquid-filled tank.

In Paper A, an antenna design with a semisolid gel made of salt (NaCl), water, and agar to mimic the effects of antennas operating in a lossy bath is presented [97], [100]. The goal was not to completely eliminate multipath signals but to attenuate them enough to prevent them from corrupting the measured signals and cause subsequent artifacts in the reconstructed images.

The antennas used for the muscle rupture detection application are shown in Figure 2.8. These are monopole antennas, fabricated by stripping the outer conductor from a semi-rigid coaxial cable. The radiating element has a length of 35 mm. To facilitate mounting, the monopole is bent at a 90° angle, allowing it to pass through a hole in the back of the plastic container. The figure also shows the gel inside the container.

The antennas were arranged in a semicircular array with a 16-cm diameter, with an angular spacing of 20° between individual antennas, as shown in Figure 2.9. The measurement system used was the Rohde & Schwarz ZNBT8,

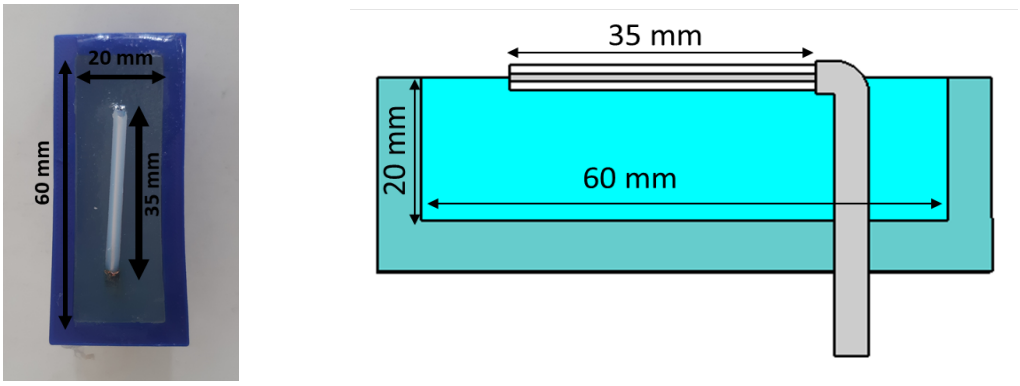

(**a**) (**b**)

Figure 2.8: Monopole antenna with cup full of gel: (**a**) top view of antenna; (**b**) side view of antenna taken from paper A.

a 16-channel vector network analyzer (VNA). This VNA offers a dynamic range of up to 140 dB and operates across a frequency range of 9 kHz to 8.5 GHz. However, for the measurements, the frequency range was limited to 0.5 GHz to 2.0 GHz. The antennas were connected to the VNA using eight flexible coaxial cables.

In Paper F and Paper G, antennas with a shorter radiating element, measuring 22 mm in length, were introduced. These were designed to operate at 1 GHz when positioned between the muscle phantom and the lossy gel, as shown in Figure 2.10a. The cup retained the same dimensions as in the previous version and the antenna were bent at a 45° angle allowing it to pass through a hole in the side of the cup. Additionally, a new antenna array featuring movable antennas, adjustable to fit different phantom or leg sizes, was introduced, as illustrated in Figure 2.10b. This new array was equipped with stepper motors, enabling the antennas to shift positions and adapt to various diameters, keeping an angular spacing of 22.5° between the antennas.

Phantoms and tissue-like media

Measurements were performed with tissue mimicking phantoms that closely replicate the permittivity and conductivity of the dielectric properties of the leg. Phantoms can be based on liquids, like glycerin [105], Triton X-100 [106] or gels [107], rubber like liquids, and solid materials [108]–[110]. In the experiments, muscle and blood phantoms manufactured from water, salt, and

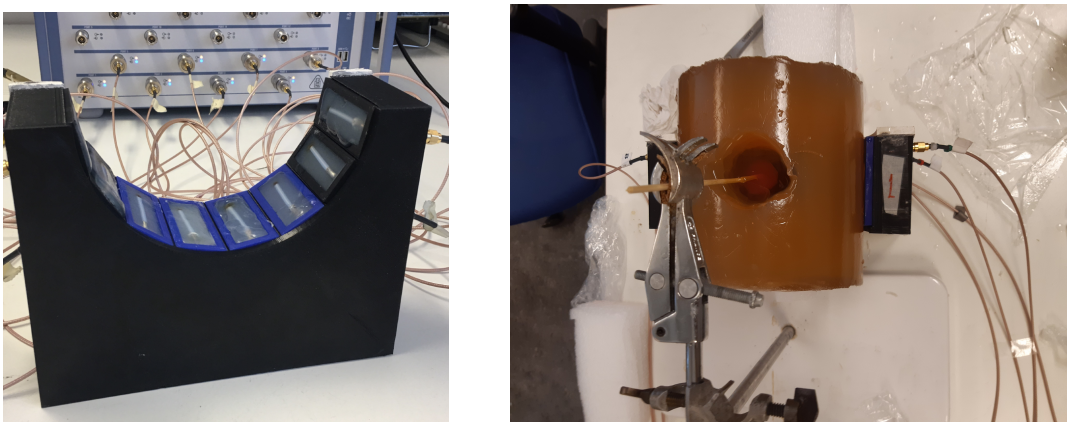

(**a**) (**b**)

Figure 2.9: Measurement setup for probe measurements and image reconstruction: (**a**) semicircular antenna array consisting of 8 antennas; (**b**) muscle phantom in the antenna array, with probes taken from paper A.

sugar were used to act as a solvent, control the conductivity, and control the permittivity, respectively. Agar was used to make the phantom solid [111]. Water, salt, and sugar were chosen because the manufacturing process is simple, the ingredients are harmless, and the mimicking of the dielectric properties of the body is sufficient for proof-of-concept experiments. Detailed descriptions of the properties and dimensions of the phantoms can be found in Paper A.

Experiments

The experiments were conducted in a simplified environment using two tissue-mimicking phantoms: one for muscle and another for blood. The muscle-mimicking material modeled the leg of the patient, while the blood-mimicking material represented the bleeding associated with muscle rupture. For simplicity, other tissues in the leg, such as fat, bone, and skin, were not included. The muscle and blood phantoms are shown in Figure 2.9b.

During the measurements, the antennas were placed in direct contact with the surface of the muscle phantom, ensuring that the monopole elements were also directly in contact with the phantom.

To investigate the effects of the different attenuating properties of the gel two different gels were manufactured: a low-loss made from regular tap water

(**a**) (**b**)

Figure 2.10: New monopole antenna and antenna array used in paper F: (**a**) top view of antenna with cup full of gel; (**b**) adjustable antenna array.

and 1.5 weight percent (wt%) agar; and a high-loss gel made from a mixture of tap water, 1.5 wt% agar and 10 wt% NaCl. The low-loss gel had permittivity $\varepsilon = 79.54$ and conductivity $\sigma = 0.235$ S/m and the high-loss gel had permittivity $\varepsilon = 61.37$ and conductivity $\sigma = 11.98$ S/m at 1 GHz. More details about the phantoms and gels are given in paper A.

Figure 2.11 shows a few examples of the measured transmission coefficients (S21 and S41) for the low-loss and high-loss gel. The first notable observation is that the amplitude measured with the high-loss gel was lower than that for the low-loss gel. The figure shows this for channels S21 and S41, but the same trend was seen for all measured channels. Another observation is that the curve for the high-loss gel is much smoother than for the low-loss gel. The measured S-parameters of the low-loss gel showed a strongly alternating amplitude that appeared to be caused by the multipath waves interfering with the desired object response.

In paper A it is further shown that the field amplitude inside the muscle phantom was preserved while the multipath signals propagating along paths outside the muscle phantom were dampened when using the high-loss gel. The lower amplitude seen in this figure for the high-loss gel is a sign that the multipath signals had been substantially reduced and the scattering amplitudes from the phantom preserved.

As shown in Figure 2.11, the low-loss gel had a low conductivity and, there-

fore, a significant level of multipath signals around the system is expected. These signals interfere with each other and make the signals unpredictable as any small change in the experimental setup can create large fluctuations in the measured signals.

2.7 Chapter Summary and Conclusions

This chapter described the development of a microwave imaging system for muscle rupture detection, focusing on advancements in antenna design and exploring the measurement quality of software-defined radios (SDRs). The significant challenge of stabilizing the phase measurement by developing a calibration strategy for the SDR was adressed. A novel approach to antenna design was introduced, utilizing simple monopole antennas arranged in a semi-circular array and coupled with a semisolid gel made of saline water and agar, which effectively attenuates multipath signals without requiring full immersion of the leg. Experimental validation using tissue-mimicking phantoms for muscle and blood demonstrated the system's potential, with the high-loss gel proving particularly effective in reducing interference while preserving the field amplitude inside the muscle phantom. By creating an adaptable antenna array with adjustable positioning and implementing sophisticated signal processing techniques, the research provides a promising proof-of-concept for non-invasive muscle rupture detection, showcasing significant potential for future clinical applications in medical imaging.

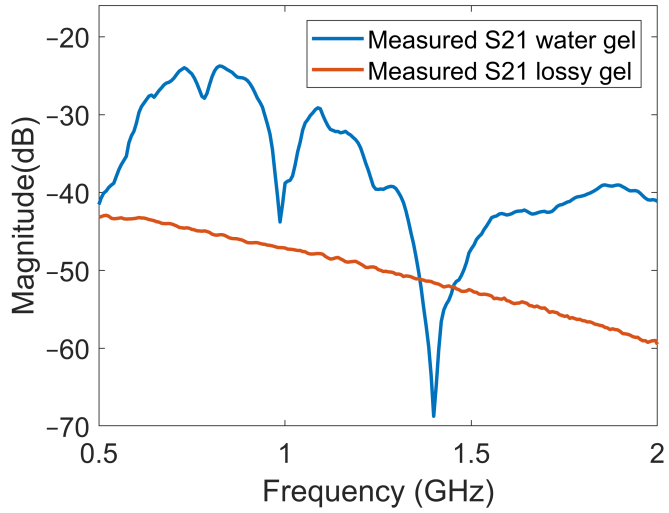

(**a**)

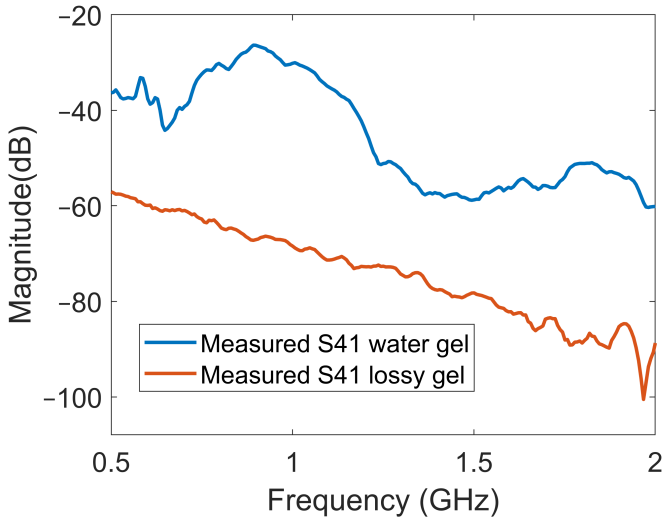

(**b**)

Figure 2.11: Comparison of transmission coefficients obtained from measured data for low loss and high loss gel : (**a**) results for S21; (**b**) results for S41.

CHAPTER 3

Imaging

Microwave imaging can be broadly categorized into two main approaches: qualitative and quantitative. Both rely on the interaction of electromagnetic waves with tissue interfaces of differing dielectric properties. These interactions cause partial transmission and reflection of the waves, leading to changes in their amplitude and phase. Antenna systems capture these variations, which are then processed to create an image.

This chapter is divided into two parts. The first part provides a concise overview of qualitative and quantitative imaging algorithms, which represent the current state of the art in microwave imaging. The second part focuses on the specific approach adopted in this work, outlining the contributions of this thesis and presenting results from the image reconstructions.

Part I: Imaging Algorithms; State of the Art

Microwave imaging can be classified into two main approaches: reconstructing patterns and shapes (qualitative imaging) or reconstructing the spatial distribution of the dielectric properties (quantitative imaging). Qualitative methods are often referred to as radar-based or confocal imaging, while quantitative methods are commonly known as tomographic imaging.

This part starts with an introduction to tomographic imaging, focusing on some of the widely used algorithms in this approach. Thereafter an overview of radar-based imaging techniques and the typical algorithms are given. Lastly, early-time content removal algorithms are discussed as this is essential for enhancing image accuracy by isolating object responses from dominant signal artifacts.

3.1 Tomographic Algorithms

Tomographic algorithms reconstruct the dielectric properties of the imaging domain using principles of inverse scattering. These algorithms often involve non-linear and iterative optimization algorithms for the image reconstruction and require solving two types of electromagnetic numerical problems: forward and inverse problems. In the forward problem, the electromagnetic propagation in a medium with known dielectric properties and antenna array is calculated; this is a relatively straightforward problem that can be solved with and several commercial solvers are available. The forward problem can be solved using a variety of different methods such as the Finite-Difference Time Domain (FDTD) method [112], [113], the Finite Element method (FEM) [114], [115], Method of Moments (MoM) [116] or the Discrete Dipole Approximation (DDA) [59], [117].

In the inverse problem, the task is to calculate the properties of the dielectric medium based on measured (or simulated) electromagnetic waves that have propagated through the medium between pairs of antennas in the array; this problem is harder to solve since the relationship between the dielectric properties in the imaging domain and the scattered field, in general, is non-linear. Several different iterative methods have been developed and used in microwave tomographic applications, like the Time-Domain Inversion Algorithm [60], the Distorted Born Iterative Method [118], Newton-based methods

[119], and Contrast Source Inversion (CSI) [120].

The iterative inversion methods use simulated electric fields in addition to measured electric fields. In each iteration, a dielectric distribution is updated incrementally from the previous iteration. The simulated fields are compared to the measured fields and the dielectric distribution is updated so the difference between the simulated and measured fields is minimized. Through repeated iterations, the dielectric distribution is adjusted such that it converges towards the original distribution.

Non-linear reconstruction algorithms require large computational resources and reconstruction times can be very long, up to many hours for 3D reconstructions. This is clearly unfeasible, particularly in clinical settings where real time imaging is more practical. Real time performance is particularly challenging for three-dimensional (3D) imaging, whereas [117] two dimensional (2D) reconstructions in real time are more feasible [59].

3.2 Radar Based Algorithms

Radar based microwave imaging is a conceptually different approach to reconstruct an image. These algorithms exploit time-of-flight measurements of pulses that are transmitted through and scattered by high dielectric contrast objects in the imaging domain [121]. Unlike microwave tomography, where the aim is to reconstruct the dielectric parameters within the object, radar based algorithms aim at only reconstructing information on the shape, size, and location of scatterers [122].

Although providing less detailed information about the object, radar based algorithms are less complex and an image can usually be reconstructed faster compared to a tomographic algorithm. These techniques typically rely on ultra-wideband pulses that are transmitted into the imaging domain to detect reflections and scattered pulses from strong dielectric scatterers [42].

The radar algorithms use estimated propagation times between pairs of antennas and individual pixels in the imaging domain. If a scatterer is present in a particular pixel the correlation between scattered signals from different directions is high; if a scatterer is not present the correlation is low. An image of the scatterer is created by repeating this process for each pixel in the region of interest. Therefore, if the signals have been processed correctly (the early time content removed), the highest intensity point in this intensity map will

correspond to the location of the dielectric scatterer [123].

Several imaging algorithms have been reported in the literature and a few examples of such algorithms are the Delay-And-Sum (DAS) [46], [122], Delay-multiply-And-Sum (DMAS) [124], Microwave Imaging via Space Time (MIST) [125], Generalized Likelihood Ratio Test (GLRT) [126], Standard Capon Beamformer(SCB) [127], [128], and Multistatic Adaptive Microwave Imaging (MAMI) beamformer [129].

Despite the fact that these algorithms are conceptually much simpler than quantitative tomographic algorithms, many challenges remain with this approach. A particular challenge is processing the received signals efficiently. The early-time content is primarily originating from reflections off the skin in the case of reflection signals, or by the direct path between antennas in transmission signals. Neither the skin reflection nor the direct path signals provide information about the object, as they represent the first response path the signal can take. On the other hand, the late-time content is dominated by the object's response, which is the desired information for imaging.

The early-time content needs to be removed from the signal before imaging. Otherwise, the desired object response will be drowned in the early-time content, which usually have a much higher amplitude than the late-time content. Improper removal of the early-time signal can lead to inaccurate reconstructions, where artifacts appear or the position of the object is misrepresented.

3.3 Early-Time Content Removal Algorithms

Different methods can be applied to remove or reduce the early-time content. One method includes the use of a priori measurements of a ttissue like phantom that resembles the object under tests such as lesion-free phantoms, or healthy tissue [124]. An alternative is to use the average of all signals recorded at each channel to estimate the early-time content [46], rotation subtraction [85] and the use of different adaptive filtering algorithms [130], [131].

The a priori data method requires that a reference signal has been obtained from measurements of healthy tissue. The reference signal is then subtracted from the signal with the object response and since the only change between the healthy and injured signals is the object (in or case blood) then the resulting signal only contains the late time content with the object response. For experimental investigations on phantoms, it is usually possible to perform these

before and after measurements. In our experiments on a muscle phantom both a healthy model (reference) and a phantom model of a ruptured muscle (a blood phantom was inserted in the muscle phantom) was measured. The reference signal was subtracted from the signal of the ruptured muscle model to generate the differential signal used as input for the imaging algorithm.

In practice, this solution would be suitable in scenarios such as monitoring of ongoing bleedings or during the rehabilitation period as it allows signal comparison over time from the same patient. However, depending on the clinical application, the use of a priori data may not always be practical, as it requires baseline measurements of the patient taken before the injury occurred. In such cases, alternative methods like rotation subtraction or adaptive filtering algorithms may be more appropriate.

These algorithms aim to estimate the early-time skin response so it can be removed from the signals before reconstructing the image [132]. Therefore, they are sensitive to measurement variability and noise in the scattering data. Even a small change can create errors or uncertainties in the estimation and removal of the early time signal that could also corrupt the late time object response that one intends to preserve. One important step to help mitigate these problems is to reduce the variability in measurement data and to keep the signals free from undesired scattering that originates from other sources than inside the body.

Part II: Contributions and Imaging Results

In this part, the impact of multipath signals on the image quality is investigated and it is shown how the use of high-loss gels behind the antennas improve the image reconstruction accuracy and repeatability. This approach reduces the variability in the measurement data, which in turn decreases the artifacts in the reconstructed images. However, in some cases, substantial background artifacts can still appear in the images. To address this, a matched filter-based DMAS algorithm has been proposed with the purpose to increase the Signal-to-Clutter Ratio (SCR) of the reconstructed images.

A majority of the imaging experiments were made with a multiport Vector Network Analyzer (VNA). Experiments were also made with a Software-Defined Radio (SDR). The SDR is a two-port system that was used to perform measurements in the frequency domain. A switching matrix had to be used to step through all desired antenna combinations. Methods to reduce the number of measured channels was investigated by analyzing how the number of transmission channels and frequency points impacted the reconstruction accuracy. This could in turn enable reduced measurment times. Finally, imaging based on the SDR measurements were demonstrated and analyzed.

3.4 Multipath Signals Deteriorate Reconstructed Images

As explained in Chapter 2, multipath signals are a significant challenge in microwave imaging, often introducing unwanted artifacts in the reconstructed images. In this section the impact of these signals is investigated and it is demonstrates how a high-loss gel can mitigate their effects. By attenuating external signal pathways and reducing measurement variability, the high-loss gel improves the repeatability and accuracy of image reconstructions. Image reconstruction results using low-loss and high-loss gels in the antennas are shown. These results confirm that use of high-loss gels behind the antennas has a substantial effect on the image reconstruction repeatability.

As discussed in Chapter 2.6 and findings detailed in paper A, an antenna design has been proposed that incorporates a semisolid, high-loss gel. This design reduces variability in measured S-parameters by effectively attenuating signals traveling outside and around the muscle phantom while preserving the

field amplitude within the phantom itself. This reduced variability translates into improved consistency in the reconstructed images, as demonstrated in paper A.

In paper A image reconstruction experiments were also done based on phantom measurements. In the experiments a blood phantom with a diameter of 4 cm was inserted at a position 3 cm above the bottom of the phantom.

For comparison two datasets were measured: one with the low-loss gel and one with the high-loss gel. For each gel, 15 measurements were taken as a priori measurement (before adding the blood that represents the muscle rupture) and 15 measurements with the blood phantom inserted into the muscle phantom. This means that for each gel, 15 differential signals could be obtained and used as the input signal to the DMAS algorithm. The reason for using multiple measurements (15) was to gather some statistics on the variability in the reconstructed images using the two different gels.

Figure 3.1 shows a few selected reconstructions that were obtained with the measured data for the low-loss gel and the high-loss gel. The reconstructions from the measured data with the low-loss gel showed great variability between images. On the other hand, the reconstructions based on measurements with the high-loss gel showed fewer artifacts in the background and the blood phantom was always reconstructed in the correct position.

For the case with low-loss gels, the reconstruction were sometimes successful as in the upper image. However with stronger artifacts close to the bottom edge compared to the images obtained using the high-loss gels. In other images the artifacts were on the other hand even larger in amplitude than the blood phantom.

Instead of showing all 15 image reconstruction a plot of the reconstructed amplitude were drawn at the vertical line crossing through the center of the muscle phantom. The reconstructed amplitudes are shown in Figure 3.2 and they show the same pattern discussed before.

In paper B the work of paper A was confirmed and extended using blood phantoms with different sizes and positions.

3.5 Matched Filter DMAS

The work in paper A and B marks a significant step forward in applying microwave imaging to sports medicine, as well as to improve other diagnostic

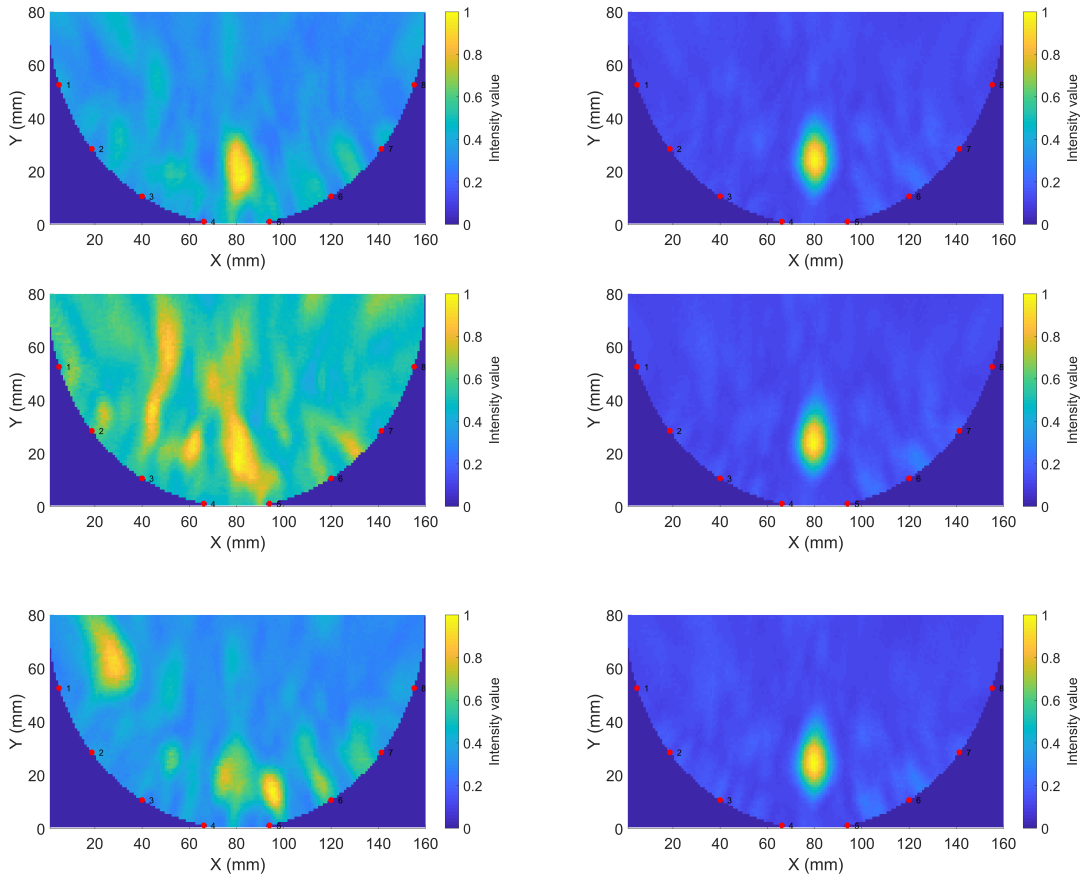

(**a**) Low-loss gel (**b**) High-loss gel

Figure 3.1: Sample reconstructions using phantom measurements: (**a**) low-loss gel; (**b**) high-loss gel. The images are reproduced from paper A.

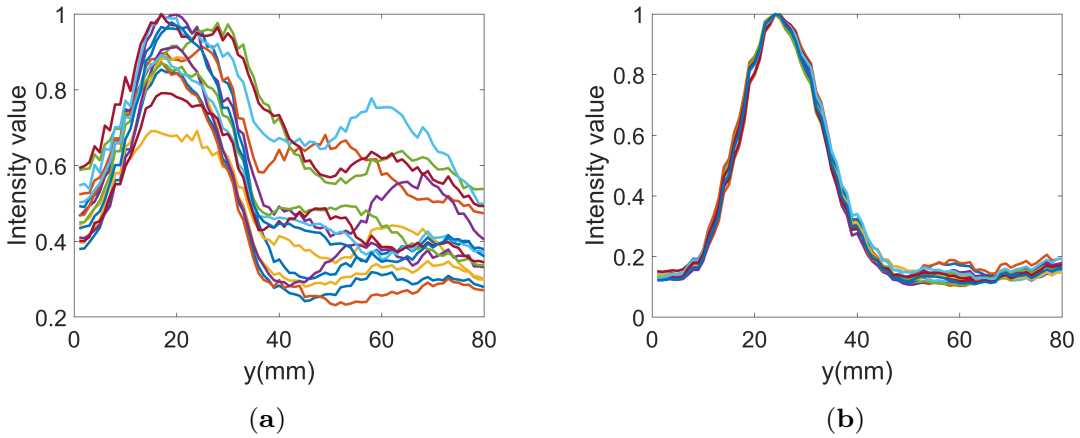

Figure 3.2: Reconstructed data along the line through the center of the imaging domain for 15 images: (**a**) low-loss gel; (**b**) high-loss gel. The images are reproduced from paper A.

applications. Despite this success, a persistent challenge is identified: the presence of substantial background artifacts in the images, particularly in cases where the blood is located deep into the muscle. These artifacts can potentially complicate the overall image interpretation and mask subtle diagnostic information. While the current method effectively locates blood accumulations, reducing background artifacts is important for enhancing image clarity, improving the signal-to-clutter (SCR) ratio in the images, and ultimately increasing the diagnostic accuracy of the imaging technique. Inspired by the matched filtering techniques an additional stage to the DMAS algorithm was introduced in paper E. The purpose was to enhance the Signal-to-Noise Ratio (SNR) of the measured signals. This enhancement, in turn, increases the Signal-to-clutter-ratio (SCR) of the reconstructed images.

In conventional radar systems, matched filtering is an effective method used to enhance the (SNR) [133]–[135]. A matched filter maximizes the SNR by optimally correlating the received signal with the expected signal [133]. A filter based on this correlation will improve the ability of a radar system to extract meaningful information from noisy signals.

The matched filter is designed to be the time-reversed complex conjugate of the expected signal. Mathematically, for a transmitted signal $s(t)$, the matched filter's impulse response $h(t)$ is given by [136]:

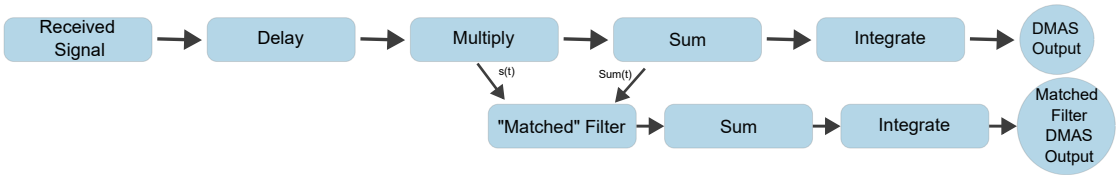

Figure 3.3: Visual representation of DMAS algorithm and proposed modification. The image is reproduced from paper E.

$$h(t) = s^*(-t), \tag{3.1}$$

where s^* denotes the complex conjugate. The output of the matched filter, $y(t)$, is the convolution of the received signal $r(t)$ with the filter's impulse response:

$$y(t) = \int r(\tau)h(t-\tau)\mathrm{d}\tau \tag{3.2}$$

Another way to explain this operation is that it computes the cross-correlation between the received signal and the expected signal template [133].

While some previous methodologies have suggested employing a matched filter to mitigate early-time clutter caused by the skin [137]–[139], the work presented in this thesis takes a different approach. The proposed method extends the traditional DMAS algorithm in three key steps. First, the received signals undergo the standard DMAS process of delay and multiplication. Second, an additional stage is introduced where the sum of these processed signals serves as the impulse response for a new filter. Third, this filter is applied to the signals as illustrated in Figure 3.3. This way the multiplied and summed signals become $h(t)$ and this filter is then applied to all the multiplied signals before summing and integrating.

Phantom Object Measurements and Metrics for Image Evaluation

The study encompassed four measured cases (the same cases as in Paper A and B), which were also simulated numerically to facilitate comparison. Figure 3.4 illustrates the measurement configurations, depicting the muscle phantom along with the size and position of the blood phantom.

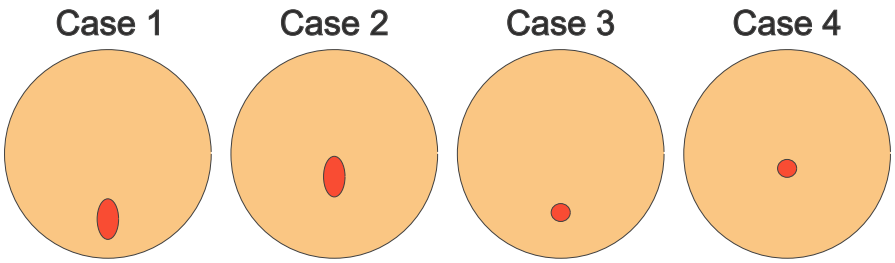

Figure 3.4: Illustration of muscle phantom and blood phantom and positions (cases). The image is reproduced from paper E.

The accuracy of the reconstructed images was analyzed with an artifact to object metric. The target region (Ω_b) was defined as the area inside the full-width at half maximum (FWHM) boundary of the peak value of the reconstructed bleeding and the pixels outside this region were defined as the clutter region (Ω_c).

Signal-to-Clutter ratio (SCR),

$$SCR = 20 * \log_{10} \left(\frac{\langle I_r(\Omega_b) \rangle}{\langle I_r(\Omega_c) \rangle} \right) \tag{3.3}$$

Here $\langle \cdot \rangle$ is the average and in an accurately reconstructed image, the SCR is high.

Image Reconstruction with the Matched Filter DMAS

Reconstructed images from measured case 4 are shown in Figure 3.5. This case results in the lowest SCR and is caused by the small size of the blood phantom and its position deep inside the muscle phantom tissue.

Reconstruction are shown with the standard DMAS algorithm (Figure 3.5a) and the matched filter DMAS approach (Figure 3.5b). To aid interpretation, all images include a dotted red circle indicating the actual shape of the blood phantom. Additionally, the full-width half-maximum (FWHM) regions of the reconstructed objects are indicated with red dotted lines and the maximum intensity pixel position is marked.

In both cases, the reconstructions accurately show the phantom's position without introducing clutter that could be mistaken for an object. However, the images reconstructed with our matched filter DMAS algorithm exhibit noticeably less clutter compared to those produced by the standard DMAS.

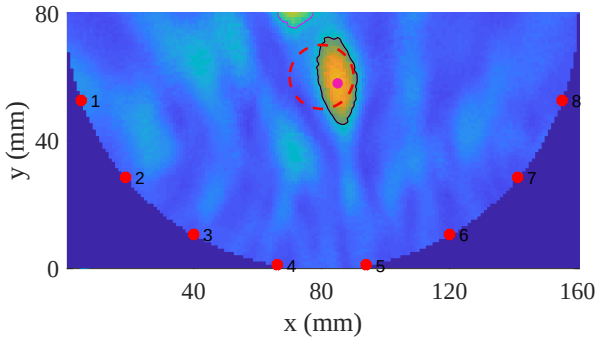

(**a**)

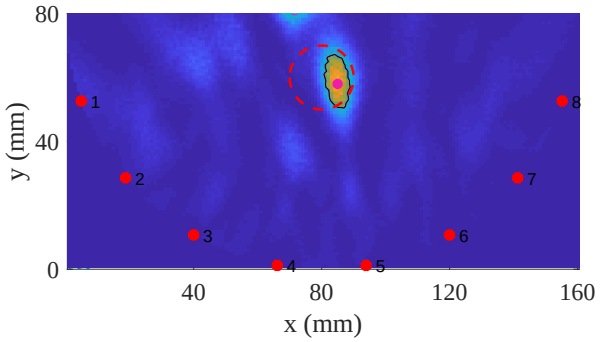

(**b**)

Figure 3.5: Reconstructed images using measured case 4 using (a) DMAS (b) our modified DMAS. The images are reproduced from paper E.

To quantify the improvement, the SCR has been calculated using eq 3.3. Figure 3.6 shows the results of the four cases. Consistently, significant SCR improvements was seen when using the matched filter DMAS, with a 16 dB increase in SCR in case 4. Clearly the matched filter DMAS significantly attenuates clutter compared to the standard DMAS algorithm, but it does not completely eliminate it.

3.6 Reduction of Measurement Time

As mentioned before, a goal is also to replace the VNA with the SDR to enable a more compact system at a lower price. Encouraged by the results in Paper C, where the measurement quality of the SDR for medical applications was

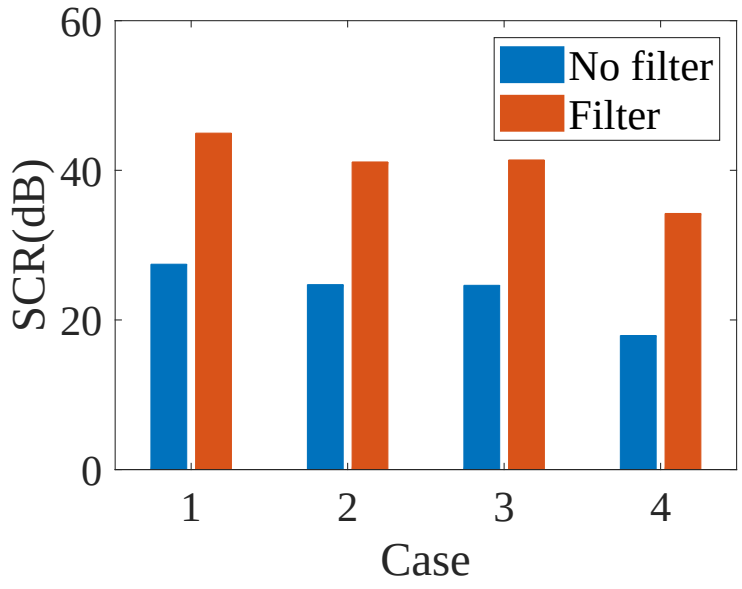

Figure 3.6: SCR of the four measured cases using the standard DMAS algorithm (No filter) and our modified version (Filter). Taken from paper E.

studied, imaging experiments were conducted in Paper F. However, a notable challenge with a SDR, and other compact systems like a 2-port VNA over a multi-port VNA, with capacity to measure several channels in parallell, is the increased measurement time. There are two main reasons for this: first a switching matrix has to be used to step through the desired antenna combinations pairwise in sequence, adding additional measuring time for each transmission channel measured. The second reason for increased measurement time is the number of frequency points as the SDR essentially operated in the frequency domain, measuring one frequency at a time. The total measurement time is therefore significantly impacted by the number of measured frequencies in the frequency range. The number of measured frequency points also impact the measurement time in a multi-port VNA, however to a lesser extent.

Long measurement times come with a risk of introducing movement artifacts in the reconstructed images due to patient movements. Consequently the number measured transmission channels and frequencies should be kept as low as possible to minimize the measurement time.

Reduction of Transmission Channels

The number of channels have a direct impact on the total measurement time. In paper D the accuracy of the reconstructed images was investigated and in fact found to be improved by a reduction of the number of transmission channels.

In this study the hypothesis was that the antennas located farther apart contain less useful information due to lower coherency between the channels, increased signal attenuation, and high noise levels. If the hypothesis is true, data from these channels could be excluded or not measured at all, thereby reducing the total number of measured channels without significantly affecting image reconstruction accuracy.

Figure 3.7 shows the reconstructed images of Case 1 when the number of transmission channels used in the reconstructions was reduced. In each figure, four examples show the reconstructions when reducing the number of transmission channels to 56, 50, 36, and 14 channels. It is seen that the reconstructions of the blood phantoms are relatively similar when making small reductions in the number of channels. However, when using only 14 transmission channels for the reconstructions the amount of clutter is significantly increased. This might lead to the false conclusion that there is more than one reconstructed bleeding.

The SCR for the four measured cases were calculated and plotted against the total number of transmission channels, as shown in Figure 3.8. This indicates that is feasible to decrease the number of transmission channels from 56 down to 36 channels while limiting the reduction in SCR to less than 12%, as channels positioned farther from the target contribute less information and more noise compared to closer channels.

Reduction of Frequency Points

As previously explained, another factor contributing to increased measurement time is the number of frequency points measured. To reduce measurement time, the number of frequency points could be reduced as much as possible without compromising the image quality significantly. This motivation led to the study presented in Paper G, where the influence of the number of frequency points on the synthesis of input time-domain signals for the DMAS algorithm was examined, and how this impacts the accuracy of

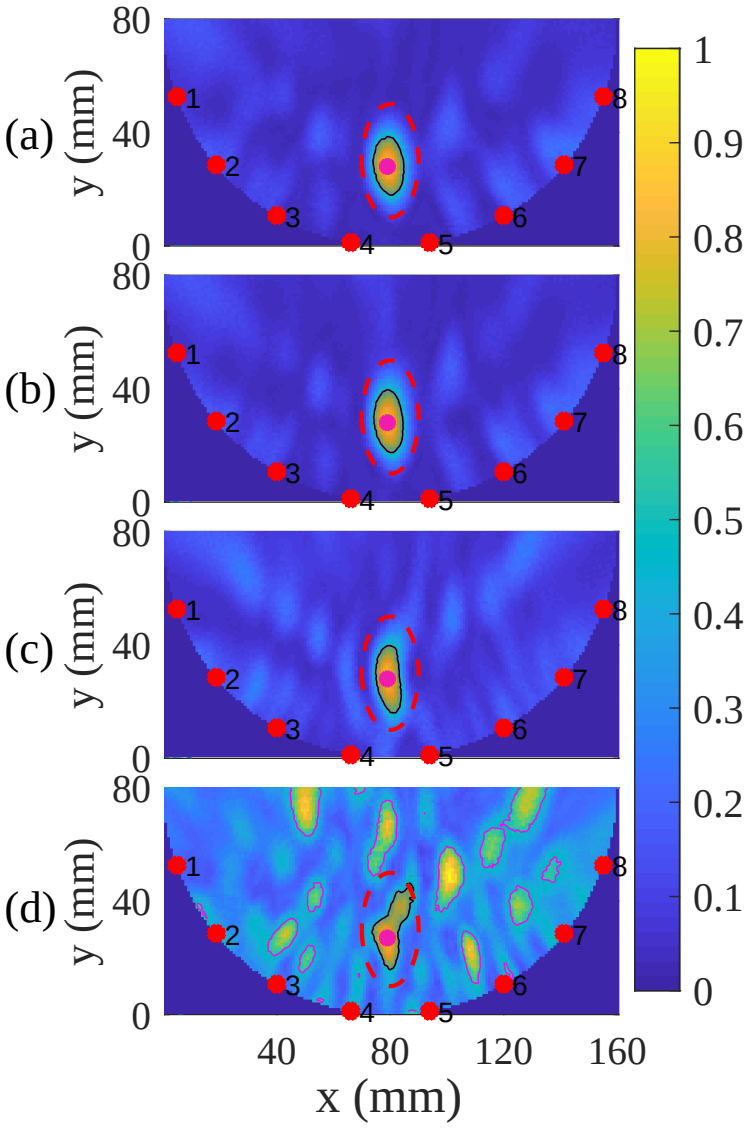

Figure 3.7: Reconstructed images of measured simulated case 1 using (a) 56 channels (b) 50 channels (c) 36 channels (d) 14 channels. The image is reproduced from paper D.

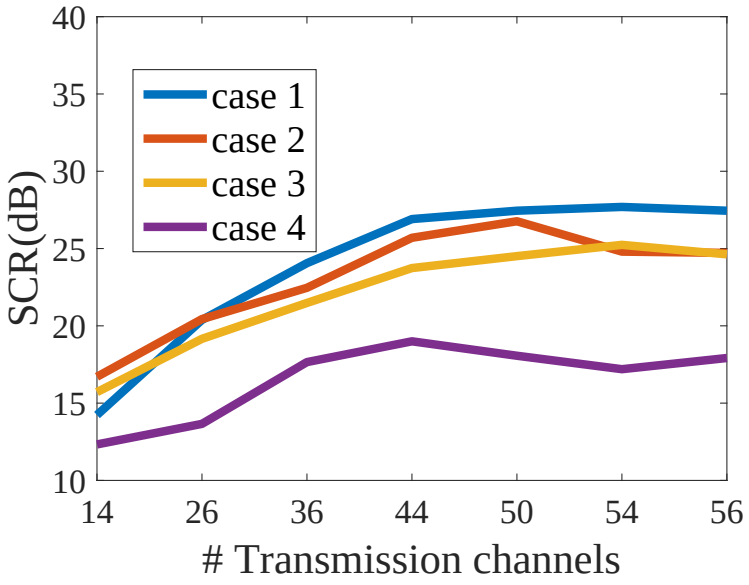

Figure 3.8: SCR for the 4 measured cases. The image is reproduced from paper D.

the reconstructed DMAS images was investigated. This study also utilized the antennas with gels and measurement system introduced in Section 2.6.

Figure 3.9 shows the reconstructed images while using 260, 13 and 6 frequency points. The position of the antennas has been modified to agree with the real position in the new antenna array. The red rectangles in these images outline the true position of the blood phantom. The reconstructed image using all 260 measured frequencies (Figure 3.9) shows two distinct intensity peaks within the expected target location. Even as the number of frequency points decreases, the reconstructions remain highly similar to the original. With as few as 13 frequencies (Figure 3.9b), the image closely resembles the one created with 260 frequencies. However, noticeable deterioration only becomes evident when the number of frequencies is reduced to six (Figure 3.9c).

3.7 Image Reconstructions Using SDR

Building on the previous discussion of Software-Defined Radios (SDRs) in Chapter 2, this section discusses their application in image reconstruction.

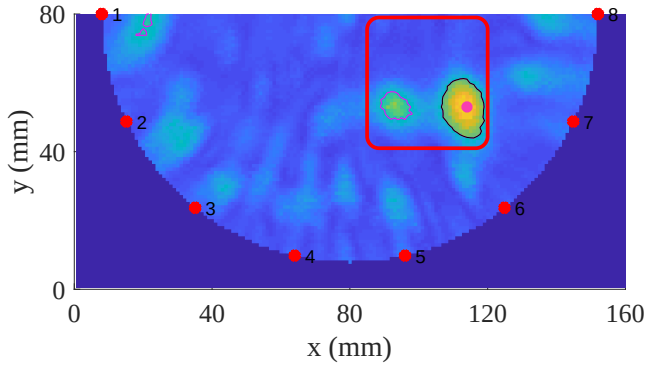

(**a**)

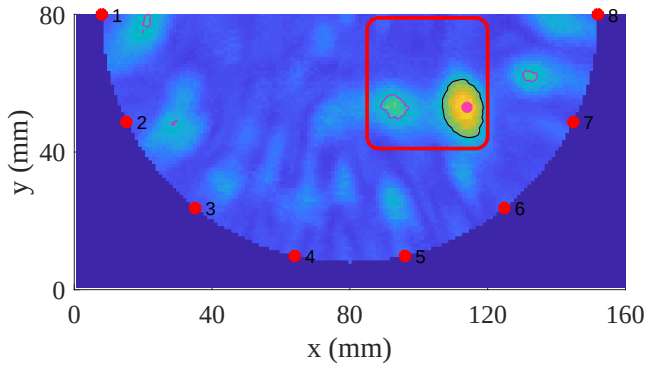

(**b**)

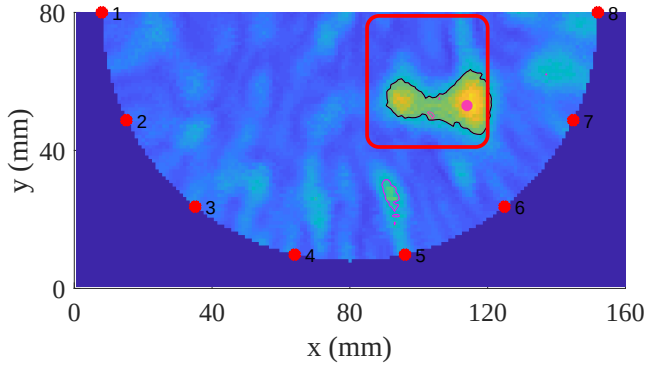

(**c**)

Figure 3.9: Reconstructions made with different numbers of frequencies in the time domain signal synthetization: (**a**) 260 frequency points; (**b**) 13 frequency points; (**b**) 6 frequency points. The images are reproduced from paper G.

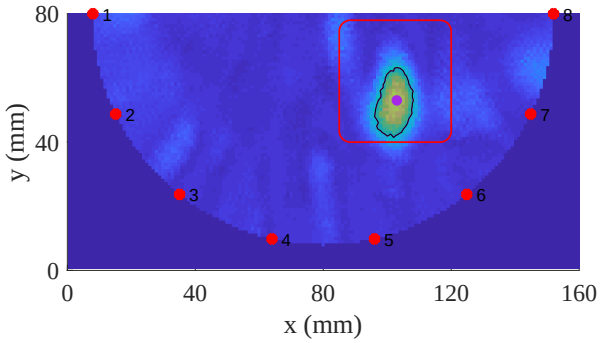

(**a**)

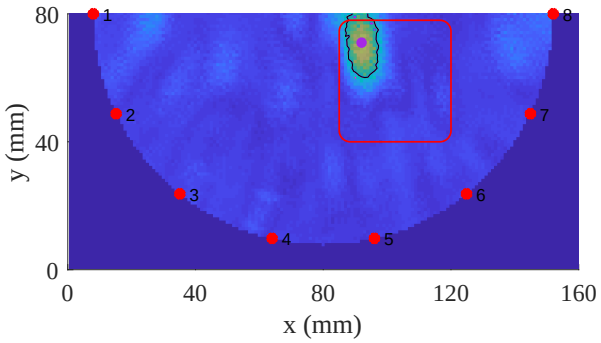

(**b**)

Figure 3.10: Reconstructions made with measurements using:(**a**) the VNA; (**b**) The SDR. The images were reproduced from paper F.

As demonstrated in Paper C, the SDR's measurement capabilities are such that image reconstruction is possible. Encouraged by these findings, in Paper F, the investigation was extended to an imaging experiment.

For the SDR measurements, the same setup as described in Section 3.4 was used, which included both a muscle phantom and a blood phantom. The differential signal between measurements with and without the blood phantom was used to reconstruct the images. Additionally, VNA measurements of the same setup were taken to serve as a benchmark for comparison.

Figure 3.10 shows the reconstructions using both the VNA and the SDR for one of the measured cases presented in Paper F. The red rectangle indicates the true position and size of the blood phantom.

The VNA-based reconstructions show the reconstructed phantom at a po-

sitioned approximately in the center of the ground truth blood phantom position. In contrast, the SDR reconstructions are off-centered, but still track the phantom's position. As seen in the image, the intensity maximum is shifted upwards and towards the center of the imaging domain. The reason for this is caused by the contributions from the farthest transmitter-receiver channels. As discussed in Chapter 2.5, these channels do not provide meaningful information about the object; instead, they mainly capture the leaked transmitted signal. When these channels are excluded from the reconstruction, the object position moves closer to the correct location of the blood phantom, as shown in Fig. 3.11c. In this figure, the reconstruction using all transmission channels, Figure 3.11cb, is positioned closer to the center of the imaging domain, while excluding the farthest channels, as done in Paper D (Section 3.6), and using 36 channels for the reconstruction, causes the intensity maximum to shift closer to the actual position of the blood phantom, Figure 3.11cc. For comparison the reconstruction made with VNA data is shown in Figure 3.11ca.

3.8 Chapter Summary and Conclusions

This chapter presents significant advancements in microwave imaging, particularly for medical diagnostics. It demonstrates how the use of high-loss gels mitigates multipath signals, reducing variability in image reconstructions and improving repeatability by attenuating external signal pathways. The introduction of an enhanced DMAS algorithm, incorporating a matched filter stage, results in a substantial improvement in the Signal-to-Clutter Ratio (SCR) of up to 17.5 dB, significantly reducing background artifacts and enhancing image clarity. Furthermore, strategies to optimize measurement time are explored, showing that transmission channels and frequency points can be reduced without major compromises in image quality when using the VNA. Specifically, reducing the number of transmission channels from 56 to 36 results in less than a 12% reduction in SCR, and the number of frequency points can be cut to 13 within the desired frequency range without significant changes in the reconstructed images. Additionally, the feasibility of performing image reconstructions using SDR measurements, following the established calibration strategies, is demonstrated.

These findings contribute to the development of more accurate and cost-effective diagnostic tools, particularly for detecting muscle ruptures and inter-

nal bleeding, with implications for sports medicine and beyond. The proven effectiveness of high-loss gels, the SCR improvement through matched filtering, and the successful application of SDRs pave the way for more portable and affordable imaging systems, enhancing both diagnostic speed and accuracy. Ultimately, this research lays a solid foundation for future advancements in microwave imaging technology, offering the potential for faster, more accessible, and precise medical diagnostics.

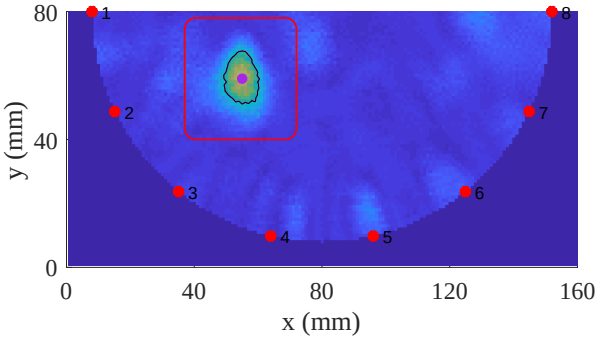

(**a**)

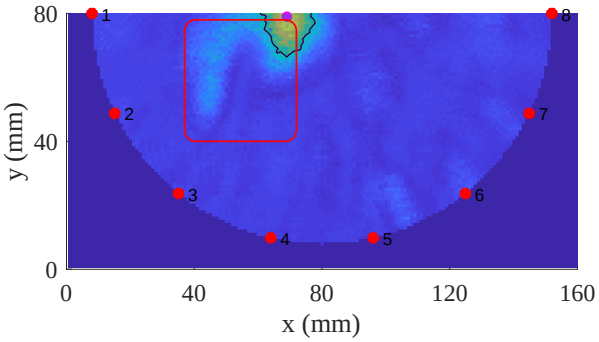

(**b**)

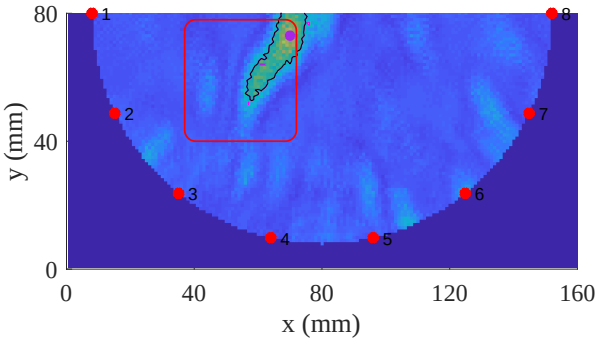

(**c**)

Figure 3.11: Reconstructions made with measurements using: (**a**) the VNA with all transmission channels; (**b**) The SDR with one external amplification stage using all available transmission channels; (**c**) The SDR with one external amplification stage but excluding the farther transmission channels. Image reproduced from paper F.

CHAPTER 4

Summary of included papers

This chapter provides a summary of the included papers, detailing both their content and the author's specific contributions.

4.1 Paper A

Laura Guerrero Orozco, Lars Peterson, Andreas Fhager
Microwave Antenna System for Muscle Rupture Imaging with a Lossy Gel to Reduce Multipath Interference
Published in Sensors 2022, 22, 4121

This paper presents a novel antenna design and a microwave antenna system for imaging with the purpose of detecting and diagnosing muscle ruptures. A conductive gel was introduced on the back and side of the antennas to attenuate the outgoing and sideways moving waves. The aim was to reduce undesired multipath signals and improve the image reconstruction accuracy. Tissue-mimicking phantoms, representing muscle and blood, were used in measurements with both low conductivity (low loss) and high conductivity (high

loss) gels at the back of the antennas. For comparison, corresponding simulations were performed as well. The results obtained from both the simulated and experimental data were in good agreement. They showed that the field amplitudes on the transmission coefficients between antennas decreased with an increased conductivity of the gel. At the same time, only a minor change in the field strength inside the muscle phantom was seen. This confirms that surface waves and other multipath waves are attenuated without significantly affecting the waves propagating through the object. Additionally, in repeated image reconstruction experiments using the DMAS beamformer algorithm, the high-loss gel antennas showed a more stable and repeatable image reconstruction accuracy in comparison to the low-loss gel. Therefore, we conclude that a reduction in the multipath signals made the signals less corrupted with unpredictable artifacts due to unwanted multipath scattering.

Contribution
The author of this thesis has performed all modelling, all experiments, performed image reconstruction, performed the analysis and written the manuscript.

4.2 Paper B

Laura Guerrero Orozco, Lars Peterson, Andreas Fhager
Muscle Rupture Microwave Imaging with a Lossy Gel to Reduce Multipath Interference
Published in 2023 17th European Conference on Antenna and Propagation (EuCAP), pp.1-5
 DOI: 10.23919/EuCAP57121.2023.10133732.

This paper presents an expansion of the results found in Paper A with the investigation expanded to different blood phantom sizes and positions. Measurements were performed using tissue-mimicking phantoms together with both a low-loss gel and a high-loss gel. Two different blood phamtom sizes were used as well as two different positions inside the muscle phantom. The results confirmed the conclusions found in paper A in different imaging scenarios and showed that reconstructions made with the high-loss gel were more repeatable and stable than those made with the low-loss gel, with respect to both phantom size and position.

Contribution
The author of this thesis has performed all modelling, all experiments, performed image reconstruction, performed the analysis and written the manuscript.

4.3 Paper C

Xuezhi Zeng, **Laura Guerrero Orozco**
Measurement quality of a software defined radio system for medical diagnostics
Published in the Journal of Engineering-JOE, Volume 2022, Issue 12 December 2022 Pages 1162-1172

The paper presents a study on the measurement accuracy of a software-defined radio (SDR) system. The aim was to investigate whether it could be used in microwave applications for medical diagnostics. The accuracy and noise levels of the measurements are critical and are directly related to diagnostic accuracy. Particularly, the high-loss characteristics of biological tissues make the measurements challenging. An extensive investigation of a single-board, two-channel USRP 2901 SDR from National Instruments is conducted. This SDR is equivalent to the Ettus Research USRP B210 board. Measurements were performed on an antenna system as well as on a variable attenuator with a 70 dB adjustable attenuation range. This attenuation range is similar to a realistic measurement scenario in any medical diagnostics application. The signal-to-noise ratio (SNR) of the measurements was also studied. Previous simulation work showed that an SNR over 15 dB is sufficient for the reconstruction of a specific breast model when using a time-domain tomography approach. In this work, we showed that this level of SNR can be obtained. Additionally, we found that the performance of the SDR is superior to a custom-built pulsed time-domain system, which usually has a maximum SNR of about 40 dB in the investigated frequency range. Furthermore, a calibration strategy is developed to calibrate the random phase caused by the two separate PLLs in the transmitter and receiver channels. We showed that we could perform stable phase measurements with the proposed calibration strategy. We also found that there was good measurement repeatability and accuracy of the SDR measurements when benchmarking against a high-performance VNA for a transmission loss of up to 70 dB.

Contribution
The author of this thesis has taken part in performing the measurements, wrote the LabView code to control the experiments, performed the data analysis, and reviewed the manuscript.

4.4 Paper D

Laura Guerrero Orozco, Lars Peterson, Andreas Fhager
Microwave imaging with a reduced number of transmission channels in a semi-circular antenna array
Submitted to IEEE-JERM 2024.

This paper investigates reducing the number of transmission channels and evaluating its impact on reconstruction accuracy. This is of interest as a reduced number of measurement channels would enable a corresponding reduction in the measurement time of low-cost, portable microwave imaging systems. Such a system is most likely constructed with a two-port microwave transceiver system. In that case, a switching matrix is needed to select transmitter-receiver antenna pairs before the measurement. Reducing the number of channels is therefore a key aspect in reducing the overall measurement time. In this study, we also compared the performance of circular and semicircular antenna arrays. The results showed that a semicircular array is sufficient for detecting the blood associated with muscle ruptures. Although this configuration slightly alters the shape of the reconstructed object, it does not compromise detection accuracy. Building on these findings, we hypothesized that antennas positioned closer together contribute more significantly to accurate reconstruction. This is likely due to their stronger signals, higher coherency, and lower noise levels compared to more distant antennas. As a result, the farthest antennas could be excluded from both measurements and reconstructions without major performance losses. We used both simulation and measurement data in the investigation. The results showed that the number of transmission channels could be reduced from 56 to 36 in the semicircular antenna array with only minor deterioration of the reconstruction accuracy. The corresponding decrease in the Signal-to-Clutter Ratio (SCR) was found to be less than 12%.

Contribution
The author of this thesis has performed all modelings, all experiments, performed image reconstruction, data analysis as well as written the manuscript.

4.5 Paper E

Laura Guerrero Orozco, Lars Peterson, Andreas Fhager
Matched Filter Enhanced Delay Multiply and Sum for Muscle Rupture Microwave Imaging
Manuscript in preparation for submission.

This paper addresses a significant challenge in microwave imaging by developing an innovative approach to reduce background artifacts in reconstructed images. We propose a modified Delay-Multiply and Sum (DMAS) algorithm that incorporates a matched filter-inspired stage, significantly enhancing the image reconstruction accuracy. The matched filter DMAS algorithm amplifies blood response signals while reducing background clutter in the image. Both simulations and measurements were used to study the performance of the algorithm across a frequency range of 0.5–1.5 GHz. The results were promising, with the new method achieving significant improvements in the signal-to-clutter ratio (SCR), increasing it by 16–17 decibels across the test cases compared to a conventional DMAS algorithm. This enhancement provides clearer, more focused images that maintain accurate localization of blood accumulations within muscle tissue. This technique demonstrates particular effectiveness in reducing artifacts in challenging scenarios, such as when the blood phantom is small and located deeper within the muscle phantom. Future work will focus on testing the technique with more complex phantoms that more closely mimic real clinical conditions, including multi-tissue scenarios and more diverse imaging contexts.

Contribution
The author of this thesis independently came up with the idea of improving the DMAS imaging algorithm with a matched filter, developed the idea, performed all experiments, image reconstruction, and data analysis as well as wrote the manuscript.

4.6 Paper F

Laura Guerrero Orozco, Xuezhi Zeng, Andreas Fhager
Microwave Imaging of Muscle Ruptures with Software Defined Radio
Manuscript in preparation for submission,.

This paper investigates the possibility of using the Software Defined Radio (SDR) for microwave imaging of muscle ruptures. The proposed system includes a semicircular antenna array, a switching matrix to change between transmission channels, a power splitter to divide the transmitted signal fo our calibration strategy, an amplifier stage to lift the signals above the leakage level from transmitter to receiver and one SDR unit as the measurement system. Experiments were done with tissue mimicking phantoms of muscle and blood and the system is able to detect the blood phantom and we are able to get image reconstructions, with results benchmarked against results obtained with the vector netwrok analyzer (VNA). While positional inaccuracies in reconstructed images were observed, the findings confirm the potential of SDR-based microwave imaging as a cost-effective, portable diagnostic tool, paving the way for further refinement and clinical adoption.

Contribution
The author of this thesis has written all codes to control the SDR experimental procedure as well as performed all experiments, performed the image reconstructions, performed the data analysis and wrote the manuscript.

4.7 Paper G

Andreas Fhager, **Laura Guerrero Orozco**, Lars Peterson
A Study on the Reduction of Frequency Points in Muscle Rupture Microwave Imaging in a semi-circular antenna array
Accepted for publication at the 19th European Conference on Antenna and Propagation, 2025.

Our work with microwave image reconstructions is based on the DMAS algorithm. This algorithm takes time-domain signals as input, and these signals are synthesized from frequency domain measurements. When using a stepped frequency domain measurement procedure, a reduction in the number of points would correspond to a reduction in the overall measurement time.

In this paper, we study the relation between the reconstruction accuracy and the number of measured frequency points. Our study demonstrates that the number of frequency points can be significantly reduced without severely compromising image quality. By systematically decreasing the frequency points from 260 to as low as 20, the relative squared error of the reconstructed image increased by less than 1Measurements were conducted using a semi-circular antenna array and tissue-mimicking phantoms, with blood phantoms introduced to replicate ruptures. This approach supports the development of low-cost diagnostic tools, paving the way for more widespread adoption of microwave imaging in sports medicine and beyond.

Contribution

The author of this thesis has performed the measurements, written the code for signal processing and image reconstructions as well as reviewed the manuscript.

CHAPTER 5

Conclusions and Future Work

This thesis provided an overview of the background and results of research towards a microwave imaging system for muscle rupture detection. The goal was to develop an imaging system capable of detecting and diagnosing muscle injuries with the potential to complement, or eventually replace, current imaging modalities such as MRI.

The research focused on developing a system that is capable of delivering repeatable measurements, is compact, and facilitates short operation times at high image accuracy.

5.1 Improving Measurement Repeatability

In the first part of this thesis, strategies to enhance measurement repeatability were investigated. In Paper A, a novel antenna system was introduced, based on a lossy gel to attenuate unwanted multipath signals. This setup significantly reduced undesired fields outside the object under test while minimally affecting signal levels within the object. Image reconstruction experiments using the DMAS algorithm demonstrated that antennas paired with this gel produced more stable and repeatable results compared to those using a low-

loss gel. Paper B extended and confirmed these findings with blood phantoms of varying sizes and positions. The conclusion was that reduction of unwanted signals outside the object under test is essential for the performance of the microwave imaging system.

For cases involving smaller, deeper bleedings in muscle phantoms, substantial background artifacts were observed, which were less prevalent in larger or more superficial bleedings. This challenge motivated the development of a method to minimize these artifacts. In Paper E, inspired by the methodology of matched filters, an additional stage to the DMAS algorithm was proposed. This stage enhanced the signal-to-clutter ratio (SCR) by up to 17.5 dB, substantially reducing background artifacts.

5.2 Compact and Affordable System Design

Another objective was to investigate methods that allow for the design of a compact and cost-effective system. Therefore, the measurement quality of a software-defined radio (SDR) as an alternative to the bulky and expensive multiport Vector Network Analyzer (VNA) was explored in Paper C. Results showed that the SDR delivered sufficient signal-to-noise ratio (SNR) for microwave imaging, and a calibration strategy was developed to stabilize the phase. Building on this, Paper F demonstrated successful image reconstructions using the SDR. While the reconstructed images showed slight positional skew, their alignment corresponded to the actual blood phantom positions, confirming the feasibility of the SDR for our system. This marked a critical step toward reducing system cost and size.

5.3 Reducing Measurement Time

With the SDR operating as a two-port frequency-domain system, a switching matrix was used to select the desired combination of transmitter-receiver combinations. In an imaging experiment, it is necessary to sequentially step through the desired channels, which, depending on the settings, could be a very time-consuming process. Minimizing the measurement time therefore became crucial. Two strategies were explored through VNA-based experiments. In Paper D, the number of transmission channels was reduced from 56 to 36 in a semicircular antenna array, which resulted in less than a 12% reduction

in SCR. In Paper G, the number of frequency points was reduced, and it was found that reducing the number of points from 260 to just 13 had no significant impact on the image accuracy.

5.4 Concluding Remarks and Future Work

This work demonstrates the feasibility of a cost-effective and accessible microwave imaging system for muscle injury detection. By addressing critical limitations of current modalities, it paves the way for broader adoption of microwave imaging in medical diagnostics. Continued innovation and collaboration will be essential to fully realize its potential and transform patient care.

Future work includes developing an early-time content removal algorithm to eliminate the dependence on prior measurements of healthy tissue. This would make the imaging process more versatile and applicable in scenarios where baseline measurements are unavailable or impractical. Implementing such an algorithm could also improve system usability in clinical settings, allowing for faster and more straightforward diagnostics.

Additionally, future studies should employ more anatomically realistic phantoms and patient models to investigate the impact of surrounding tissues, such as bone and fat, on image reconstruction. These tissues could introduce additional challenges, such as signal scattering and attenuation, which need to be addressed to ensure the system's reliability and accuracy in real-world applications. Exploring these factors will bring the technology closer to clinical translation by ensuring robustness in diverse and complex anatomical conditions

References

[1] F. Arroyo, "Overview of different location of muscle strain," *Muscle Injuries in Sport Medicine*, 2013.

[2] L. Peterson and P. Renström, *Skador Inom Idrotten: Prevention, behandling och rehabilitering*. Columbus Förlag, 2017.

[3] P. Volpi, G. Melegati, D. Tornese, and M. Bandi, "Muscle strains in soccer: A five-year survey of an italian major league team," *Knee Surgery, Sports Traumatology, Arthroscopy*, vol. 12, no. 5, 2004.

[4] C. M. Askling, M. Tengvar, T. Saartok, and A. Thorstensson, "Acute first-time hamstring strains during high-speed running," *The American Journal of Sports Medicine*, vol. 35, no. 2, pp. 197–206, 2007.

[5] K. M. Cross, K. K. Gurka, M. Conaway, and C. D. Ingersoll, "Hamstring strain incidence between genders and sports in ncaa athletics," *Athletic Training amp; Sports Health Care*, vol. 2, no. 3, pp. 124–130, 2010.

[6] J. Karlsson and R. Jerre, "The use of radiography, magnetic resonance, and ultrasound in the diagnosis of hip, pelvis, and groin injuries," *Sports Medicine and Arthroscopy Review*, vol. 5, no. 4, pp. 268–273, Oct. 1997.

[7] J. M. Koscso, K. McElheny, J. B. Carr, and K. J. Hippensteel, *Lower extremity muscle injuries in the overhead athlete - current reviews in musculoskeletal medicine*, Aug. 2022.

[8] C. M. Askling, G. Koulouris, T. Saartok, S. Werner, and T. M. Best, "Total proximal hamstring ruptures: Clinical and mri aspects including guidelines for postoperative rehabilitation," *Knee Surgery, Sports Traumatology, Arthroscopy*, vol. 21, no. 3, pp. 515–533, 2012.

[9] D. A. Connell, M. E. Schneider-Kolsky, J. L. Hoving, *et al.*, "Longitudinal study comparing sonographic and mri assessments of acute and healing hamstring injuries," *American Journal of Roentgenology*, vol. 183, no. 4, pp. 975–984, 2004.

[10] G. Koulouris and D. Connell, "Hamstring muscle complex: An imaging review," *RadioGraphics*, vol. 25, no. 3, pp. 571–586, 2005.

[11] J. Albayda, G. Demonceau, and P. G. Carlier, "Muscle imaging in myositis: Mri, us, and pet," *Best Practice & Research Clinical Rheumatology*, vol. 36, no. 2, p. 101 765, 2022, Inflammatory Myositis, ISSN: 1521-6942.

[12] L. Mica, A. Schwaller, C. Stoupis, I. Penka, J. Vomela, and A. Vollenweider, "Avulsion of the hamstring muscle group: A follow-up of 6 adult non-athletes with early operative treatment: A brief report," *World Journal of Surgery*, vol. 33, no. 8, pp. 1605–1610, 2009.

[13] S. K. Chu and M. E. Rho, "Hamstring injuries in the athlete," *Current Sports Medicine Reports*, vol. 15, no. 3, pp. 184–190, 2016.

[14] C. M. Askling, N. Malliaropoulos, and J. Karlsson, "High-speed running type or stretching-type of hamstring injuries makes a difference to treatment and prognosis," *British Journal of Sports Medicine*, vol. 46, no. 2, pp. 86–87, 2012, ISSN: 0306-3674.

[15] R. Drake, *Gray's anatomy for students*. Elsevier, 2020.

[16] L. Devlin, "Recurrent posterior thigh symptoms detrimental to performance in rugby union," *Sports Medicine*, vol. 29, no. 4, pp. 273–287, 2000.

[17] B. Blaus. "File: `Pulled Hamstring.png`." Wikimedia Commons [Accessed: 05/09/24]. (2015), [Online]. Available: `https://commons.wikimedia.org/wiki/File:Pulled_Hamstring.png`.

[18] B. Palmer, M. McBride, G. Jones, and L. Mayhew, "415 injury trends in men's english professional football: An 11 year case series," *British Journal of Sports Medicine*, vol. 55, no. Suppl 1, A158–A158, 2021, ISSN: 0306-3674.

[19] J. Ekstrand, M. Hägglund, and M. Waldén, "Injury incidence and injury patterns in professional football: The uefa injury study," *British Journal of Sports Medicine*, vol. 45, no. 7, pp. 553–558, 2011, ISSN: 0306-3674.

[20] C. Woods, "The football association medical research programme: An audit of injuries in professional football–analysis of hamstring injuries," *British Journal of Sports Medicine*, vol. 38, no. 1, pp. 36–41, 2004.

[21] J. Orchard and H. Seward, "Epidemiology of injuries in the australian football league, seasons 1997–2000," *British Journal of Sports Medicine*, vol. 36, no. 1, pp. 39–44, 2002.

[22] P. Edouard, B. Caumeil, C. Giroux, *et al.*, "Epidemiology of injury complaints in elite sprinting athletes in athletics (track and field)," *Applied Sciences*, vol. 13, no. 14, 2023, ISSN: 2076-3417.

[23] P. Edouard and J. Alonso, "Epidemiology of track and field injuries," *New Studies in Athletics · no. 1./2.2013*, vol. 28, pp. 85–92, Jan. 2013.

[24] N. Malliaropoulos, T. Isinkaye, K. Tsitas, and N. Maffulli, "Reinjury after acute posterior thigh muscle injuries in elite track and field athletes," *The American Journal of Sports Medicine*, vol. 39, no. 2, pp. 304–310, 2010.

[25] J. Petersen, "Evidence based prevention of hamstring injuries in sport," *British Journal of Sports Medicine*, vol. 39, no. 6, pp. 319–323, 2005.

[26] P. Edouard, P.-E. Dandrieux, S. Iatropoulos, *et al.*, "Injuries in athletics (track and field): A narrative review presenting the current problem of injuries," *German Journal of Sports Medicine*, vol. 74, no. 4, pp. 132–141, Jun. 2024.

[27] J. H. Brooks, C. W. Fuller, S. P. Kemp, and D. B. Reddin, "Incidence, risk, and prevention of hamstring muscle injuries in professional rugby union," *The American Journal of Sports Medicine*, vol. 34, no. 8, pp. 1297–1306, 2006.

[28] C. McCuller, R. Jessu, and A. L. Callahan, "Physiology, skeletal muscle," *StatPearls [Internet].*, Jul. 2023.

[29] *Smart servier medical art*, `https://smart.servier.com/` [Accessed: 05/09/24], Jul. 2024.

[30] H.-W. Mueller-Wohlfahrt, L. Haensel, K. Mithoefer, *et al.*, "Terminology and classification of muscle injuries in sport: The munich consensus statement," *British Journal of Sports Medicine*, vol. 47, no. 6, pp. 342–350, 2012.

[31] M. Kjaer, M. Krogsgaard, P. Magnusson, *et al.*, *Textbook of sports medicine basic science and clinical aspects of sports injury and physical activity*. John Wiley & Sons, 2008.

[32] M. Conforti, "The treatment of muscle hematomas," in *Muscle Injuries in Sport Medicine*, G. N. Bisciotti and C. Eirale, Eds., Rijeka: IntechOpen, 2013, ch. 7.

[33] D. A. L. Bass, "Sport and medicine: Rehabilitation after soft tissue trauma," *Proceedings of the Royal Society of Medicine*, vol. 59, no. 7, pp. 653–656, 1966.

[34] W. E. Garret, F. R. Rich, P. K. Nikolaou, and J. B. Vogler, "Computed tomography of hamstring muscle strains," *Medicine amp; Science in Sports amp; Exercise*, vol. 21, no. 5, 1989.

[35] G. M. Verrall, J. P. Slavotinek, P. G. Barnes, and G. T. Fon, "Diagnostic and prognostic value of clinical findings in 83 athletes with posterior thigh injury," *The American Journal of Sports Medicine*, vol. 31, no. 6, pp. 969–973, 2003.

[36] C. M. Askling, M. Tengvar, T. Saartok, and A. Thorstensson, "Acute first-time hamstring strains during high-speed running," *The American Journal of Sports Medicine*, vol. 35, no. 2, pp. 197–206, 2007.

[37] H. Seward, J. Orchard, H. Hazard, and D. Collinson, "Football injuries in australia at the élite level," *Medical Journal of Australia*, vol. 159, no. 5, pp. 298–301, 1993.

[38] J. Buckley and J. Aler, "Enhancements in the determination of ocean surface wave height from grazing incidence microwave backscatter," in *IGARSS '98. Sensing and Managing the Environment. 1998 IEEE International Geoscience and Remote Sensing. Symposium Proceedings. (Cat. No.98CH36174)*, vol. 5, 1998, 2487–2489 vol.5.

[39] N. K. Nikolova, "Microwave imaging for breast cancer," *IEEE Microwave Magazine*, vol. 12, no. 7, pp. 78–94, 2011.

[40] G. Gennarelli, G. Vivone, P. Braca, F. Soldovieri, and M. G. Amin, "Multiple extended target tracking for through-wall radars," *IEEE Transactions on Geoscience and Remote Sensing*, vol. 53, no. 12, pp. 6482–6494, 2015.

[41] A. Joisel, J. Mallorqui, A. Broquetas, *et al.*, "Microwave imaging techniques for biomedical applications," in *IMTC/99. Proceedings of the 16th IEEE Instrumentation and Measurement Technology Conference (Cat. No.99CH36309)*, vol. 3, 1999, 1591–1596 vol.3.

[42] E. C. Fear, "Microwave imaging of the breast," *Technology in Cancer Research & Treatment*, vol. 4, no. 1, pp. 69–82, 2005.

[43] C. Gabriel, S. Gabriel, and E. Corthout, "The dielectric properties of biological tissues: I. literature survey," *Physics in Medicine and Biology*, vol. 41, no. 11, pp. 2231–2249, 1996.

[44] S. Gabriel, R. W. Lau, and C. Gabriel, "The dielectric properties of biological tissues: III. parametric models for the dielectric spectrum of tissues," *Physics in Medicine and Biology*, vol. 41, no. 11, pp. 2271–2293, 1996.

[45] P. Meaney, M. Fanning, D. Li, S. Poplack, and K. Paulsen, "A clinical prototype for active microwave imaging of the breast," *IEEE Transactions on Microwave Theory and Techniques*, vol. 48, no. 11, pp. 1841–1853, 2000.

[46] X. Li and S. Hagness, "A confocal microwave imaging algorithm for breast cancer detection," *IEEE Microwave and Wireless Components Letters*, vol. 11, no. 3, pp. 130–132, 2001.

[47] E. C. Fear, J. Bourqui, C. Curtis, D. Mew, B. Docktor, and C. Romano, "Microwave breast imaging with a monostatic radar-based system: A study of application to patients," *IEEE Transactions on Microwave Theory and Techniques*, vol. 61, no. 5, pp. 2119–2128, 2013.

[48] S. Y. Semenov and D. R. Corfield, "Microwave tomography for brain imaging: Feasibility assessment for stroke detection," *International Journal of Antennas and Propagation*, vol. 2008, pp. 1–8, 2008.

[49] M. Persson, A. Fhager, H. D. Trefná, *et al.*, "Microwave-based stroke diagnosis making global prehospital thrombolytic treatment possible," *IEEE Transactions on Biomedical Engineering*, vol. 61, no. 11, pp. 2806–2817, 2014.

[50] L. E. Larsen and J. H. Jacobi, "Microwave scattering parameter imagery of an isolated canine kidney," *Medical Physics*, vol. 6, no. 5, pp. 394–403, 1979.

[51] S. Y. Semenov, A. E. Bulyshev, V. G. Posukh, Y. E. Sizov, T. C. Williams, and A. E. Souvorov, "Microwave tomography for detection/imaging of myocardial infarction. i. excised canine hearts," *Annals of Biomedical Engineering*, vol. 31, no. 3, pp. 262–270, 2003.

[52] A. Cannatà, A. Elahi, M. O'Halloran, *et al.*, "Microwave bone imaging: Reconstruction of anthropomorphic numerical calcaneus phantoms for bone diseases diagnosis," *IEEE Access*, vol. 12, pp. 123 447–123 458, 2024.

[53] P. M. Meaney, D. Goodwin, A. H. Golnabi, *et al.*, "Clinical microwave tomographic imaging of the calcaneus: A first-in-human case study of two subjects," *IEEE Transactions on Biomedical Engineering*, vol. 59, no. 12, pp. 3304–3313, 2012.

[54] S. Semenov, J. Kellam, P. Althausen, *et al.*, "Microwave tomography for functional imaging of extremity soft tissues: Feasibility assessment," *Physics in Medicine and Biology*, vol. 52, no. 18, pp. 5705–5719, 2007.

[55] K. S. Sultan, B. Mohammed, M. Manoufali, and A. M. Abbosh, "Portable electromagnetic knee imaging system," *IEEE Transactions on Antennas and Propagation*, vol. 69, no. 10, pp. 6824–6837, 2021.

[56] S. Borzooei, P.-H. Tournier, V. Dolean, *et al.*, "Numerical modeling for shoulder injury detection using microwave imaging," *IEEE Journal of Electromagnetics, RF and Microwaves in Medicine and Biology*, vol. 8, no. 3, pp. 282–289, 2024.

[57] J. C. Lai, C. B. Soh, E. Gunawan, and K. S. Low, "Uwb microwave imaging for breast cancer detection — experiments with heterogeneous breast phantoms," *Progress In Electromagnetics Research M*, vol. 16, pp. 19–29, 2011.

[58] X. Zeng, A. Fhager, P. Linner, M. Persson, and H. Zirath, "Experimental investigation of the accuracy of an ultrawideband time-domain microwave-tomographic system," *IEEE Transactions on Instrumentation and Measurement*, vol. 60, no. 12, pp. 3939–3949, 2011.

[59] S. Hosseinzadegan, A. Fhager, M. Persson, S. D. Geimer, and P. M. Meaney, "Discrete dipole approximation-based microwave tomography for fast breast cancer imaging," *IEEE Transactions on Microwave Theory and Techniques*, vol. 69, no. 5, pp. 2741–2752, 2021.

[60] A. Fhager, P. Hashemzadeh, and M. Persson, "Reconstruction quality and spectral content of an electromagnetic time-domain inversion algorithm," *IEEE Transactions on Biomedical Engineering*, vol. 53, no. 8, pp. 1594–1604, 2006.

[61] M. Klemm, I. J. Craddock, J. A. Leendertz, A. Preece, and R. Benjamin, "Radar-based breast cancer detection using a hemispherical antenna array—experimental results," *IEEE Transactions on Antennas and Propagation*, vol. 57, no. 6, pp. 1692–1704, 2009.

[62] M. Bassi, M. Caruso, M. S. Khan, A. Bevilacqua, A.-D. Capobianco, and A. Neviani, "An integrated microwave imaging radar with planar antennas for breast cancer detection," *IEEE Transactions on Microwave Theory and Techniques*, vol. 61, no. 5, pp. 2108–2118, 2013.

[63] X. Zeng, A. Fhager, Z. He, M. Persson, P. Linner, and H. Zirath, "Development of a time domain microwave system for medical diagnostics," *IEEE Transactions on Instrumentation and Measurement*, vol. 63, no. 12, pp. 2931–2939, 2014.

[64] L. Kranold, M. Taherzadeh, F. Nabki, M. Coates, and M. Popović, "Microwave breast screening prototype: System miniaturization with ic pulse radio," *IEEE Journal of Electromagnetics, RF and Microwaves in Medicine and Biology*, vol. 5, no. 2, pp. 168–178, 2021.

[65] A. T. Mobashsher, A. M. Abbosh, and Y. Wang, "Microwave system to detect traumatic brain injuries using compact unidirectional antenna and wideband transceiver with verification on realistic head phantom," *IEEE Transactions on Microwave Theory and Techniques*, vol. 62, no. 9, pp. 1826–1836, 2014.

[66] A. Santorelli, M. Chudzik, E. Kirshin, *et al.*, "Experimental demonstration of pulse shaping for time-domain microwave breast imaging," *Progress In Electromagnetics Research*, vol. 133, pp. 309–329, 2013.

[67] X. Zeng, A. Fhager, M. Persson, and H. Zirath, "Performance evaluation of a time-domain microwave system for medical diagnostics," *IEEE Transactions on Instrumentation and Measurement*, vol. 68, no. 8, pp. 2880–2889, 2019.

[68] M. Hines and H. Stinehelfer, "Time-domain oscillographic microwave network analysis using frequency-domain data," *IEEE Transactions on Microwave Theory and Techniques*, vol. 22, no. 3, pp. 276–282, 1974.

[69] Z. Maricevic, T. Sarkar, Y. Hua, and A. Djordjevic, "Time-domain measurements with the hewlett-packard network analyzer hp 8510 using the matrix pencil method," *IEEE Transactions on Microwave Theory and Techniques*, vol. 39, no. 3, pp. 538–547, 1991.

[70] E. Fear, J. Sill, and M. Stuchly, "Experimental feasibility study of confocal microwave imaging for breast tumor detection," *IEEE Transactions on Microwave Theory and Techniques*, vol. 51, no. 3, pp. 887–892, 2003.

[71] J. Sill and E. Fear, "Tissue sensing adaptive radar for breast cancer detection—experimental investigation of simple tumor models," *IEEE Transactions on Microwave Theory and Techniques*, vol. 53, no. 11, pp. 3312–3319, 2005.

[72] D. Cook, H. Brown, I. Widanapathirana, *et al.*, "Case report: Preliminary images from an electromagnetic portable brain scanner for diagnosis and monitoring of acute stroke," *Frontiers in Neurology*, vol. 12, 2021.

[73] T. Ulversoy, "Software defined radio: Challenges and opportunities," *IEEE Communications Surveys & Tutorials*, vol. 12, no. 4, pp. 531–550, 2010.

[74] M. Sadiku and C. Akujuobi, "Software-defined radio: A brief overview," *IEEE Potentials*, vol. 23, no. 4, pp. 14–15, 2004.

[75] J. Marimuthu, K. S. Bialkowski, and A. M. Abbosh, "Software-defined radar for medical imaging," *IEEE Transactions on Microwave Theory and Techniques*, vol. 64, no. 2, pp. 643–652, 2016.

[76] A. E. Stancombe, K. S. Bialkowski, and A. M. Abbosh, "Portable microwave head imaging system using software-defined radio and switching network," *IEEE Journal of Electromagnetics, RF and Microwaves in Medicine and Biology*, vol. 3, no. 4, pp. 284–291, 2019.

[77] P. Meaney, A. Hartov, T. Raynolds, *et al.*, "Low cost, high performance, 16-channel microwave measurement system for tomographic applications," *Sensors*, vol. 20, no. 18, 2020, ISSN: 1424-8220.

[78] National Instruments, *Block diagram of usrp 2901*, Available at `https://www.ni.com/docs/en-US/bundle/usrp-2901-feature/page/block-diagram.html`, Feb. 2023.

[79] M. Persson, A. Fhager, H. D. Trefná, *et al.*, "Microwave-based stroke diagnosis making global prehospital thrombolytic treatment possible," *IEEE Transactions on Biomedical Engineering*, vol. 61, no. 11, pp. 2806–2817, 2014.

[80] X. Li, M. Jalilvand, Y. L. Sit, and T. Zwick, "A compact double-layer on-body matched bowtie antenna for medical diagnosis," *IEEE Transactions on Antennas and Propagation*, vol. 62, no. 4, pp. 1808–1816, 2014.

[81] H. Bahramiabarghouei, E. Porter, A. Santorelli, B. Gosselin, M. Popović, and L. A. Rusch, "Flexible 16 antenna array for microwave breast cancer detection," *IEEE Transactions on Biomedical Engineering*, vol. 62, no. 10, pp. 2516–2525, 2015.

[82] M. Tommer, K. G. Kjelgård, and T. S. Lande, "Body coupled wideband monopole antenna," in *2016 Loughborough Antennas Propagation Conference (LAPC)*, 2016, pp. 1–5.

[83] A. M. de Oliveira, A. M. de Oliveira Neto, M. B. Perotoni, *et al.*, "A fern antipodal vivaldi antenna for near-field microwave imaging medical applications," *IEEE Transactions on Antennas and Propagation*, vol. 69, no. 12, pp. 8816–8829, 2021.

[84] X. Li, L. Zwirello, M. Jalilvand, and T. Zwick, "Design and near-field characterization of a planar on-body uwb slot-antenna for stroke detection," in *2012 IEEE International Workshop on Antenna Technology (iWAT)*, 2012, pp. 201–204.

[85] M. Klemm, I. J. Craddock, A. Preece, J. Leendertz, and R. Benjamin, "Evaluation of a hemi-spherical wideband antenna array for breast cancer imaging," *Radio Science*, vol. 43, no. 06, pp. 1–15, 2008.

[86] A. Garrido-Atienza, M. Guardiola, L. M. Neira, J. Romeu, and A. Fhager, "Movement tracking and false positive reduction method for microwave colonoscopy systems," *IEEE Journal of Electromagnetics, RF and Microwaves in Medicine and Biology*, pp. 1–7, 2024.

[87] S.-H. Son, "Preclinical prototype development of a microwave tomography system for breast cancer detection," *ETRI Journal*, vol. 32, no. 6, pp. 901–910, 2010.

[88] S. Semenov, "Microwave tomography: Review of the progress towards clinical applications," *Philosophical Transactions of the Royal Society A: Mathematical, Physical and Engineering Sciences*, vol. 367, no. 1900, pp. 3021–3042, 2009.

[89] P. M. Meaney, F. Shubitidze, M. W. Fanning, M. Kmiec, N. R. Epstein, and K. D. Paulsen, "Surface wave multipath signals in near-field microwave imaging," *International Journal of Biomedical Imaging*, vol. 2012, pp. 1–11, 2012.

[90] S. M. Pishnamaz, X. Zeng, H. D. Trefná, M. Persson, and A. Fhager, "Reducing waves on the body surface in near-field medical diagnostics by a dielectric rod antenna," *IEEE Transactions on Antennas and Propagation*, vol. 71, no. 10, pp. 7958–7969, 2023.

[91] C. J. Salomon, N. Petrović, and P. O. Risman, "Evanescent field applicator for contactless microwave breast diagnostics in air," *IEEE Transactions on Antennas and Propagation*, vol. 72, no. 7, pp. 5489–5501, 2024.

[92] A. Fhager, S. K. Padhi, M. Persson, and J. Howard, "Antenna modeling and reconstruction accuracy of time domain-based image reconstruction in microwave tomography," *International Journal of Biomedical Imaging*, vol. 2013, pp. 1–14, 2013.

[93] L. E. Larsen and J. H. Jacobi, "Microwave interrogation of dielectric targets. part i: By scattering parameters," *Medical Physics*, vol. 5, no. 6, pp. 500–508, 1978.

[94] J. H. Jacobi and L. E. Larsen, "Microwave interrogation of dielectric targets. part ii: By microwave time delay spectroscopy," *Medical Physics*, vol. 5, no. 6, pp. 509–513, 1978.

[95] Y. Fang, K. Bakian-Dogaheh, J. Stang, A. Tabatabaeenejad, and M. Moghaddam, "A versatile and shelf-stable dielectric coupling medium for microwave imaging," *IEEE Transactions on Biomedical Engineering*, vol. 69, no. 8, pp. 2701–2712, 2022.

[96] P. M. Meaney, "Addressing multipath signal corruption in microwave tomography and the influence on system design and algorithm development," *Open Access Journal of Biomedical Engineering and Biosciences*, vol. 1, no. 1, 2018.

[97] P. M. Meaney, C. J. Fox, S. D. Geimer, and K. D. Paulsen, "Electrical characterization of glycerin: Water mixtures: Implications for use as a coupling medium in microwave tomography," *IEEE Transactions on Microwave Theory and Techniques*, vol. 65, no. 5, pp. 1471–1478, 2017.

[98] N. Petrovic, T. Gunnarsson, N. Joachimowicz, and M. Otterskog, "Robot controlled data acquisition system for microwave imaging," in *2009 3rd European Conference on Antennas and Propagation*, 2009, pp. 3356–3360.

[99] J. Chang, K. Paulsen, P. Meaney, and M. Fanning, "Non-invasive thermal assessment of tissue phantoms using an active near field microwave imaging technique," English (US), *International Journal of Hyperthermia*, vol. 14, no. 6, pp. 513–534, 1998, ISSN: 0265-6736.

[100] J. Bourqui, J. Garrett, and E. Fear, "Measurement and analysis of microwave frequency signals transmitted through the breast," *International Journal of Biomedical Imaging*, vol. 2012, pp. 1–11, 2012.

[101] C. J. Fox, P. M. Meaney, F. Shubitidze, L. Potwin, and K. D. Paulsen, "Characterization of an implicitly resistively-loaded monopole antenna in lossy liquid media," *International Journal of Antennas and Propagation*, vol. 2008, pp. 1–9, 2008.

[102] National Instruments, *Usrp-2901*, Available at `https://www.ni.com/sv-se/support/model.usrp-2901.html`.

[103] P. Meaney, K. Paulsen, and J. Chang, "Near-field microwave imaging of biologically-based materials using a monopole transceiver system," *IEEE Transactions on Microwave Theory and Techniques*, vol. 46, no. 1, pp. 31–45, 1998.

[104] C. Gilmore, A. Zakaria, S. Pistorius, and J. LoVetri, "Microwave imaging of human forearms: Pilot study and image enhancement," *International Journal of Biomedical Imaging*, vol. 2013, pp. 1–17, 2013.

[105] P. M. Meaney, C. J. Fox, S. D. Geimer, and K. D. Paulsen, "Electrical characterization of glycerin: Water mixtures: Implications for use as a coupling medium in microwave tomography," *IEEE Transactions on Microwave Theory and Techniques*, vol. 65, no. 5, pp. 1471–1478, 2017.

[106] N. Joachimowicz, C. Conessa, T. Henriksson, and B. Duchêne, "Breast phantoms for microwave imaging," *IEEE Antennas and Wireless Propagation Letters*, vol. 13, pp. 1333–1336, 2014.

[107] M. Habibi, D. P. Klemer, and V. Raicu, "Two-dimensional dielectric spectroscopy: Implementation and validation of a scanning open-ended coaxial probe," *Review of Scientific Instruments*, vol. 81, no. 7, p. 075 108, 2010.

[108] J. Garrett and E. Fear, "Stable and flexible materials to mimic the dielectric properties of human soft tissues," *IEEE Antennas and Wireless Propagation Letters*, vol. 13, pp. 599–602, 2014.

[109] P. Meaney, K. Paulsen, S. Geimer, S. Haider, and M. Fanning, "Quantification of 3-d field effects during 2-d microwave imaging," *IEEE Transactions on Biomedical Engineering*, vol. 49, no. 7, pp. 708–720, 2002.

[110] T. Rydholm, A. Fhager, M. Persson, and P. M. Meaney, "A first evaluation of the realistic supelec-breast phantom," *IEEE Journal of Electromagnetics, RF and Microwaves in Medicine and Biology*, vol. 1, no. 2, pp. 59–65, 2017.

[111] Q. Duan, J. H. Duyn, N. Gudino, *et al.*, "Characterization of a dielectric phantom for high-field magnetic resonance imaging applications," *Medical Physics*, vol. 41, no. 10, p. 102 303, 2014.

[112] A. Fhager, S. K. Padhi, and J. Howard, "3d image reconstruction in microwave tomography using an efficient fdtd model," *IEEE Antennas and Wireless Propagation Letters*, vol. 8, pp. 1353–1356, 2009.

[113] A. Taflove and S. C. Hagness, *Computational electrodynamics: The finite-difference time-domain method*. Artech House, 2010.

[114] K. Paulsen, P. Meaney, M. Moskowitz, and J. Sullivan, "A dual mesh scheme for finite element based reconstruction algorithms," *IEEE Transactions on Medical Imaging*, vol. 14, no. 3, pp. 504–514, 1995.

[115] A. M. Abbosh, B. Mohammed, and K. S. Bialkowski, "Differential microwave imaging of the breast pair," *IEEE Antennas and Wireless Propagation Letters*, vol. 15, pp. 1434–1437, 2016.

[116] A. Franchois and C. Pichot, "Microwave imaging-complex permittivity reconstruction with a levenberg-marquardt method," *IEEE Transactions on Antennas and Propagation*, vol. 45, no. 2, pp. 203–215, 1997.

[117] T. M. Grzegorczyk, P. M. Meaney, P. A. Kaufman, R. M. diFlorio-Alexander, and K. D. Paulsen, "Fast 3-d tomographic microwave imaging for breast cancer detection," *IEEE Transactions on Medical Imaging*, vol. 31, no. 8, pp. 1584–1592, 2012.

[118] F. Gao, B. D. Van Veen, and S. C. Hagness, "Sensitivity of the distorted born iterative method to the initial guess in microwave breast imaging," *IEEE Transactions on Antennas and Propagation*, vol. 63, no. 8, pp. 3540–3547, 2015.

[119] T. Takenaka, H. Jia, and T. Tanaka, "Microwave imaging of electrical property distributions by a forward-backward time-stepping method," *Journal of Electromagnetic Waves and Applications*, vol. 14, no. 12, pp. 1609–1626, 2000.

[120] A. Zakaria, C. Gilmore, and J. LoVetri, "Finite-element contrast source inversion method for microwave imaging," *Inverse Problems*, vol. 26, no. 11, p. 115 010, 2010.

[121] M. A. Elahi, B. R. Lavoie, E. Porter, *et al.*, "Comparison of radar-based microwave imaging algorithms applied to experimental breast phantoms," in *2017 XXXIInd General Assembly and Scientific Symposium of the International Union of Radio Science (URSI GASS)*, 2017, pp. 1–4.

[122] S. Hagness, A. Taflove, and J. Bridges, "Two-dimensional fdtd analysis of a pulsed microwave confocal system for breast cancer detection: Fixed-focus and antenna-array sensors," *IEEE Transactions on Biomedical Engineering*, vol. 45, no. 12, pp. 1470–1479, 1998.

[123] S. Semenov, A. Bulyshev, A. Abubakar, *et al.*, "Microwave-tomographic imaging of the high dielectric-contrast objects using different image-reconstruction approaches," *IEEE Transactions on Microwave Theory and Techniques*, vol. 53, no. 7, pp. 2284–2294, 2005.

[124] H. Been Lim, N. Thi Tuyet Nhung, E.-P. Li, and N. Duc Thang, "Confocal microwave imaging for breast cancer detection: Delay-multiply-and-sum image reconstruction algorithm," *IEEE Transactions on Biomedical Engineering*, vol. 55, no. 6, pp. 1697–1704, 2008.

[125] E. Bond, X. Li, S. Hagness, and B. Van Veen, "Microwave imaging via space-time beamforming for early detection of breast cancer," *IEEE Transactions on Antennas and Propagation*, vol. 51, no. 8, pp. 1690–1705, 2003.

[126] S. Davis, H. Tandradinata, S. Hagness, and B. Van Veen, "Ultrawideband microwave breast cancer detection: A detection-theoretic approach using the generalized likelihood ratio test," *IEEE Transactions on Biomedical Engineering*, vol. 52, no. 7, pp. 1237–1250, 2005.

[127] P. Stoica, Z. Wang, and J. Li, "Robust capon beamforming," *IEEE Signal Processing Letters*, vol. 10, no. 6, pp. 172–175, 2003.

[128] J. Li, P. Stoica, and Z. Wang, "On robust capon beamforming and diagonal loading," *IEEE Transactions on Signal Processing*, vol. 51, no. 7, pp. 1702–1715, 2003.

[129] Y. Xie, B. Guo, L. Xu, J. Li, and P. Stoica, "Multistatic adaptive microwave imaging for early breast cancer detection," *IEEE Transactions on Biomedical Engineering*, vol. 53, no. 8, pp. 1647–1657, 2006.

[130] B. Maklad, C. Curtis, E. C. Fear, and G. G. Messier, "Neighborhood-based algorithm to facilitate the reduction of skin reflections in radar-based microwave imaging," *Progress In Electromagnetics Research B*, vol. 39, pp. 115–139, 2012.

[131] M. A. Elahi, M. Glavin, E. Jones, and M. O'Halloran, "Artifact removal algorithms for microwave imaging of the breast," *Progress In Electromagnetics Research*, vol. 141, pp. 185–200, 2013.

[132] M. A. Elahi, "Confocal microwave imaging and artifact removal algorithms for the early detection of breast cancer," Ph.D. dissertation, NUI Galway, 2018.

[133] N. Levanon and E. Mozeson, "Matched filter," in *Radar Signals*. 2004, pp. 20–33.

[134] C. Leuschen and R. Plumb, "A matched-filter-based reverse-time migration algorithm for ground-penetrating radar data," *IEEE Transactions on Geoscience and Remote Sensing*, vol. 39, no. 5, pp. 929–936, 2001.

[135] R. L. Mitchell and A. W. Rihaczek, "Matched-filter responses of the linear fm waveform," *IEEE Transactions on Aerospace and Electronic Systems*, vol. AES-4, no. 3, pp. 417–432, 1968.

[136] B. Mahafza, "The matched filter and the radar ambiguity function," in *Radar Systems Analysis and Design Using MATLAB*. Chapman and Hall/CRC, 2005.

[137] P. Kosmas and C. Rappaport, "A matched-filter fdtd-based time reversal approach for microwave breast cancer detection," *IEEE Transactions on Antennas and Propagation*, vol. 54, no. 4, pp. 1257–1264, 2006.

[138] E. Oral and A. Sahakian, "3-d microwave imaging of breast tumors with matched-filtering," in *The 26th Annual International Conference of the IEEE Engineering in Medicine and Biology Society*, vol. 1, 2004, pp. 1423–1426.

[139] A. Afsari and A. Abbosh, "Pulse compression with minimum uncertainty: An efficient microwave medical imaging technique," in *2016 International Conference on Electromagnetics in Advanced Applications (ICEAA)*, 2016, pp. 670–673.